Journal of Asian Earth Sciences 53 (2012) 151–175

Contents lists available at SciVerse ScienceDirect

Journal of Asian Earth Sciences

journal homepage: www.elsevier.com/locate/jseaes

Temporal–spatial distribution and tectonic implications of the batholiths in the Gaoligong–Tengliang–Yingjiang area, western Yunnan: Constraints from zircon U–Pb ages and Hf isotopes

Yi-Gang Xu [a,*], Qi-Jun Yang [a,b], Jiang-Bo Lan [a], Zhen-Yu Luo [a], Xiao-Long Huang [a], Yu-Ruo Shi [c], Lie-Wen Xie [d]

[a] State Key Laboratory of Isotope Geochemistry, Guangzhou Institute of Geochemistry, Chinese Academy of Sciences, Guangzhou 510640, PR China
[b] Guilin Institute of Technology, Guilin 541004, PR China
[c] Institute of Geology, Chinese Academy of Geological Sciences, Beijing 100037, PR China
[d] State Key Laboratory of Lithospheric Evolution, Institute of Geology and Geophysics, Chinese Academy of Sciences, Beijing 100029, PR China

ARTICLE INFO

Article history:
Received 21 March 2011
Received in revised form 22 May 2011
Accepted 9 June 2011
Available online 20 November 2011

Keywords:
SHRIMP dating
Hf isotope
Zircons
Granitic batholiths
Subduction
Crustal thickening
Cordilleran-style orogen
Gaoligong–Tengliang–Yingjiang belt
Western Yunnan

ABSTRACT

Considerable progress has recently been made regarding temporal and spatial distribution of magmatism in the Lhasa Terrane. However the eastward and southeastward correlation of these Tibetan magmatic suites in western Yunnan and Burma remains poorly constrained. This paper reports zircon U–Pb dating and Hf isotopic compositions of granites in the Gaoligong–Tengliang–Yingjiang area, west Yunnan. It reveals three episodes of plutonism, and more importantly a southwestward magmatic migration. The Gaoligong batholiths in the northeast were mainly emplaced during early Cretaceous (126–121 Ma) and comprised predominantly S-type granites with negative zircon εHf values ($\varepsilon_{Hf} = -2\sim-12$). The Tengliang granites, situated southwest of the Gaoligong belt, were emplaced in late Cretaceous (68–76 Ma) and also displayed a strong peraluminous affinity and negative ε_{Hf} ($-5\sim-14$), indicating a provenance from a Proterozoic sedimentary source with little mantle contribution. The youngest phase of magmatism (52–66 Ma) occurred in Yingjiang, southwestmost of the study area. It is composed of S-type granites ($\varepsilon Hf = -2\sim-12$) in east Yingjiang and I-type granites ($\varepsilon_{Hf} = -4\sim+6$) in west Yingjiang, near the China–Burma border. The late Cretaceous–early Cenozoic plutons in the Tengliang and Yingjiang area are thus considered as the northern continuation of the late Cretaceous magmatic arc (west), which comprises I-type granites and andesitic rocks, and of the belt of predominant S-type granites (east) in Burma, Thailand and Malaysia. Such a chemical polarity of the dual I-type and S-type granites is strongly reminiscent of the northern American Cordillera, indicating a Cordilleran-style continental margin during the late Cretaceous–early Cenozoic. While the magmatic arc was related to eastward subduction of the Neo-Tethys beneath the Asian continent, the S-type granites represented the melting products of thickened crust in the hinterland, in response to subduction-induced decrease in lithospheric strength and compressive plate-convergence forces and to a less degree to the collision between Burma and Sundaland blocks. The Gaoligong early Cretaceous granites, which bear strong similarities in lithology, geochemistry and emplacement age to those in the northern magmatic belt in the Lhasa Terrane, are also the magmatic expression of crustal thickening. This crustal thickening may have stemmed from the collision between the Lhasa Block and the Qiangtang Block in late Jurassic and Early Cretaceous. The magmatism in western Yunnan thus recorded a long-term subduction of the Neo-Tethyan plate, enhanced by continental collisions at different time.

1. Introduction

The large scale northward penetration of the Indian Plate into Asia since the early Cenozoic resulted in the formation of the most spectacular collisional orogen in world. This has stimulated considerable investigation into how this largest orogenic belt was formed and when the Tibetan plateau was uplifted (Tapponnier et al., 2001; Harrison et al., 1992; Turner et al., 1993; Chung et al., 1998; Yin and Harrison, 2000). Accompanied by the deformation and uplift, plutonism and volcanism occurred in the interior of the plateau, providing opportunities to characterize the magmatic response during the evolution of the Tibetan Plateau (e.g., Chung et al., 2005). Dating

* Corresponding author. Tel.: +86 20 85290109; fax: +86 20 85290261.
E-mail address: yigangxu@gig.ac.cn (Y.-G. Xu).

1367-9120/$ - see front matter © 2011 Elsevier Ltd. All rights reserved.
doi:10.1016/j.jseaes.2011.06.018

Table 1
Zircon U–Pb isotopic data of the Gaoligong–Tengliang–Yingjiang batholiths.

Spot No.	$f^{206}Pb^*$	U (ppm)	Th (ppm)	$^{232}Th/^{238}U$	$^{207}Pb/^{206}Pb$	±% (1σ)	$^{207}Pb/^{235}U$	±% (1σ)	$^{206}Pb/^{238}U$ (1σ)	±% (Ma)	$^{206}Pb/^{238}U$ (Ma)	Age
SHRIMP												
GLS-36 (98°35′07″E, 27°45′32″N)												
1.1	3.64	269	235	0.90	0.04100	34	0.1040	35	0.01827	4.4	116.7	±5.1
2.1	2.15	272	185	0.70	0.04420	12	0.1240	14	0.02030	6.5	129.7	±8.4
3.1	1.94	614	527	0.89	0.04340	11	0.1110	12	0.01852	3.8	118.3	±4.5
4.1	0.34	678	412	0.63	0.05140	4.9	0.1309	6.2	0.01846	3.8	117.9	±4.4
5.1	0.53	846	711	0.87	0.04930	4.1	0.1321	5.6	0.01942	3.8	124.0	±4.6
6.1	0.79	1123	1456	1.34	0.04670	4.8	0.1287	6.1	0.01998	3.8	127.5	±4.7
7.1	1.02	477	361	0.78	0.04860	4.6	0.1329	6.1	0.01985	3.9	126.7	±4.9
8.1	2.48	245	213	0.90	0.04820	17	0.1260	17	0.01891	4.8	120.8	±5.7
9.1	1.41	458	524	1.18	0.05470	9	0.1510	9.7	0.02002	3.8	127.8	±4.9
10.1	0.59	1003	334	0.34	0.04730	4.6	0.1279	5.9	0.01962	3.7	125.2	±4.6
11.1	0.31	1695	1082	0.66	0.04860	2	0.1358	4.2	0.02026	3.7	129.3	±4.8
12.1	0.56	491	462	0.97	0.04940	4	0.1334	5.6	0.01958	3.8	125.0	±4.7
13.1	2.59	208	179	0.89	0.05560	8.8	0.1520	9.7	0.01984	4	126.7	±5.1
14.1	0.37	714	768	1.11	0.05180	3.6	0.1450	7.8	0.02020	7	129.1	±8.9
GLS-58 (98°47′19″E, 27°09′52″N)												
1.1	0.52	1216	637	0.54	0.04720	4.5	0.1601	4.7	0.02460	1.6	156.7	±2.5
2.1	0.69	902	412	0.47	0.04830	3.3	0.1278	3.7	0.01919	1.7	122.5	±2.1
3.1	0.47	1160	581	0.52	0.05010	4	0.1325	4.5	0.01919	2	122.5	±2.5
4.1	0.46	1303	743	0.59	0.04850	3.5	0.1305	3.8	0.01951	1.5	124.6	±1.9
5.1	0.11	1070	745	0.72	0.05200	2.8	0.1398	3.3	0.01951	1.6	124.6	±2.0
6.1	0.62	1202	725	0.62	0.04870	7.4	0.1280	7.6	0.01906	1.7	121.7	±2.0
7.1	1.02	816	533	0.67	0.04490	7	0.1172	7.2	0.01892	1.7	120.8	±2.0
8.1	0.60	703	438	0.64	0.05240	5.1	0.1417	5.3	0.01961	1.6	125.2	±2.0
9.1	0.88	784	465	0.61	0.04840	6.3	0.1228	6.5	0.01840	1.8	117.5	±2.1
10.1	1.26	862	405	0.49	0.04550	5.8	0.1175	6	0.01873	1.6	119.6	±1.9
11.1	0.26	1117	587	0.54	0.04970	4	0.1321	4.3	0.01929	1.5	123.2	±1.9
12.1	0.62	1169	504	0.45	0.04470	8	0.1202	8.1	0.01951	1.5	124.6	±1.9
13.1	0.41	974	598	0.63	0.05120	3.4	0.1359	3.7	0.01924	1.5	122.8	±1.9
14.1	0.98	1391	902	0.67	0.04600	6.3	0.1219	6.5	0.01924	1.5	122.9	±1.9
15.1	1.30	803	458	0.59	0.04750	5.9	0.1201	6.1	0.01832	1.7	117.0	±2.0
GLS-62 (98°49′37″E, 27°08′01″N)												
1.1	0.67	1524	901	0.61	0.04670	4.3	0.1181	4.6	0.01832	1.6	117.1	±1.8
2.1	0.10	4538	945	0.22	0.04757	1.3	0.1241	3	0.01892	2.7	120.9	±3.3
3.1	0.23	2167	754	0.36	0.04800	2.5	0.1307	2.9	0.01976	1.5	126.2	±1.8
4.1	0.47	657	404	0.64	0.04880	3.7	0.1224	4	0.01818	1.6	116.1	±1.9
5.1	0.58	1523	1051	0.71	0.04980	4.8	0.1250	5	0.01819	1.6	116.2	±1.8
6.1	0.61	2236	851	0.39	0.04750	3.9	0.1405	4.2	0.02144	1.5	136.8	±2.0
7.1	0.39	1314	658	0.52	0.04700	3	0.1264	3.4	0.01953	1.6	124.7	±1.9
8.1	0.92	989	639	0.67	0.04970	9.4	0.1170	9.8	0.01705	2.5	109.0	±2.7
9.1	0.30	2581	778	0.31	0.04720	3.6	0.1363	3.9	0.02095	1.5	133.6	±2.0
10.1	0.16	3381	2326	0.71	0.04847	1.8	0.1157	2.5	0.01731	1.7	110.7	±1.9
11.1	0.42	1326	758	0.59	0.04760	3.8	0.1217	4.2	0.01853	1.9	118.4	±2.2
12.1	0.17	1355	571	0.44	0.04970	3.3	0.1459	3.7	0.02130	1.6	135.9	±2.2
13.1	0.41	1435	843	0.61	0.04910	3.5	0.1259	3.8	0.01859	1.5	118.7	±1.8
14.1	0.14	3406	2144	0.65	0.04980	2.2	0.1362	4.5	0.01985	3.9	126.7	±4.9
15.1	0.45	1419	622	0.45	0.04450	6	0.1079	6.2	0.01757	1.6	112.3	±1.8
16.1	0.20	3150	1710	0.56	0.04879	1.9	0.1288	2.3	0.01915	1.4	122.3	±1.7
17.1	0.32	2804	1492	0.55	0.04870	2.4	0.1295	2.8	0.01926	1.4	123.0	±1.7
18.1	0.62	1684	796	0.49	0.04980	3.6	0.1265	3.9	0.01843	1.5	117.8	±1.7
GSL-38 (98°35′07″E, 27°45′32″N)												
1.1	0.52	1262	559	0.46	0.05140	4.7	0.1438	5.5	0.02029	2.9	129.5	±3.7
2.1	0.81	1262	423	0.35	0.04700	5.4	0.0694	6	0.01071	2.5	68.7	±1.7
3.1	1.84	521	631	1.25	0.04230	11	0.1100	12	0.01883	2.5	120.2	±3.0
4.1	0.84	384	509	1.37	0.04590	6	0.1215	6.6	0.01920	2.6	122.6	±3.2
5.1	0.94	672	630	0.97	0.04480	9.8	0.1190	11	0.01926	3.8	123.0	±4.7
6.1	2.58	505	544	1.11	0.03850	15	0.1060	16	0.01990	6	127.3	±7.6
7.1	0.97	703	1089	1.60	0.04880	7.3	0.1360	7.7	0.02016	2.5	128.7	±3.2
8.1	0.66	1060	1138	1.11	0.04640	4.6	0.1297	5.2	0.02026	2.4	129.3	±3.1
9.1	2.15	484	527	1.13	0.04040	13	0.1100	13	0.01974	2.6	126.0	±3.2
10.1	0.54	632	535	0.87	0.04380	5.3	0.1192	5.9	0.01974	2.5	126.0	±3.1
11.1	1.72	360	395	1.13	0.04020	14	0.1110	15	0.02001	2.7	127.7	±3.5
12.1	1.09	339	343	1.04	0.06440	5.3	0.1625	6	0.01831	2.7	117.0	±3.1
13.1	2.20	188	197	1.08	0.06440	12	0.1730	12	0.01944	2.9	124.1	±3.5
14.1	5.81	343	364	1.10	0.02100	49	0.0540	49	0.01814	3.1	115.9	±3.5
15.1	0.00	177	167	0.98	0.06080	6.1	0.1630	6.7	0.01940	2.8	123.9	±3.5
16.1	0.46	934	780	0.86	0.04870	4.3	0.1459	4.9	0.02172	2.4	138.5	±3.3
GLS-53 (98°42′48″E, 27°12′11″N)												
1.1	1.12	2185	1200	0.57	0.04490	5.6	0.0782	6.8	0.01263	3.7	80.9	±3.0
2.1	1.29	821	413	0.52	0.05230	3.8	0.0856	7.8	0.01187	6.8	76.1	±5.1
3.1	3.00	555	378	0.70	0.04560	18	0.0680	19	0.01077	5.8	69.1	±4.0

Table 1 (*continued*)

Spot No.	$f^{206}Pb^{*}$	U (ppm)	Th (ppm)	$^{232}Th/^{238}U$	$^{207}Pb/^{206}Pb$	±% (1σ)	$^{207}Pb/^{235}U$	±% (1σ)	$^{206}Pb/^{238}U$ (1σ)	±% (Ma)	$^{206}Pb/^{238}U$ (Ma)	Age
4.1	1.53	846	558	0.68	0.04360	13	0.0676	14	0.01124	3.9	72.1	±2.8
5.1	1.52	589	324	0.57	0.05280	9.9	0.0777	11	0.01069	3.9	68.5	±2.6
6.1	0.66	2886	1509	0.54	0.04790	3.6	0.0754	5.1	0.01141	3.7	73.2	±2.7
7.1	0.16	697	870	1.29	0.07610	1.9	1.7310	5.3	0.16490	5	984.0	±45
7.2	0.52	2659	564	0.22	0.04850	3.3	0.0876	6.2	0.01310	5.2	83.9	±4.4
8.1	1.26	752	689	0.95	0.05040	5.9	0.0853	7	0.01228	3.8	78.7	±3.0
9.1	0.23	348	193	0.57	0.08250	1.7	2.7000	4.1	0.23740	3.7	1373.0	±46
9.2	0.34	2850	533	0.19	0.04430	2.8	0.0695	11	0.01140	10	72.9	±7.5
10.1	0.54	1400	518	0.38	0.05180	3.2	0.0891	4.9	0.01247	3.8	79.9	±3.0
11.1	1.89	1066	491	0.48	0.04280	12	0.0605	12	0.01026	3.8	65.8	±2.5
12.1	1.08	842	549	0.67	0.05130	7	0.0831	9.5	0.01175	6.4	75.3	±4.8
13.1	2.50	627	314	0.52	0.04810	15	0.0660	16	0.00992	6.4	63.6	±4.0
TCXL-2 (98°23′04″E, 25°25′22″N)												
1.1	4.06	463	498	1.11	0.03900	28	0.0560	28	0.01038	3.2	66.6	±2.1
2.1	1.09	2687	1687	0.65	0.04350	5.7	0.0706	6.2	0.01177	2.4	75.4	±1.8
3.1	0.55	1696	1145	0.70	0.05040	4.4	0.0828	5	0.01191	2.4	76.3	±1.8
4.1	0.35	1850	1080	0.60	0.04490	4.8	0.0709	5.4	0.01145	2.4	73.4	±1.7
5.1	1.18	1314	1005	0.79	0.04450	7.7	0.0762	8.1	0.01242	2.5	79.6	±2.0
6.1	0.20	1939	1238	0.66	0.04950	3.6	0.0778	4.3	0.01140	2.4	73.1	±1.7
7.1	1.55	806	786	1.01	0.03850	11	0.0609	12	0.01148	2.7	73.6	±1.9
8.1	0.09	2222	1360	0.63	0.04900	2.5	0.0730	6.1	0.01080	5.6	69.3	±3.9
9.1	0.61	1826	1096	0.62	0.04520	4.5	0.0734	7.9	0.01179	6.6	75.5	±4.9
10.1	2.23	1047	697	0.69	0.04150	12	0.0672	13	0.01174	2.6	75.2	±1.9
11.1	0.00	412	306	0.77	0.05910	4.5	0.0979	5.2	0.01201	2.7	77.0	±2.1
12.1	0.20	2362	1544	0.68	0.04900	2.3	0.0833	3.3	0.01235	2.4	79.1	±1.9
13.1	3.42	310	307	1.03	0.03900	17	0.0620	17	0.01143	2.9	73.3	±2.1
14.1	0.24	2392	1254	0.54	0.04710	2.9	0.0799	3.8	0.01229	2.4	78.7	±1.9
15.1	1.91	520	399	0.79	0.04150	14	0.0621	15	0.01085	2.7	69.6	±1.9
TCBH-6 (98°15′21″E, 25°05′52″N)												
1.1	0.72	1627	874	0.56	0.04810	5.1	0.0752	5.3	0.01133	1.7	72.6	±1.2
2.1	0.17	1544	753	0.50	0.05450	3.2	0.0900	7.6	0.01198	6.9	76.8	±5.2
3.1	1.04	1539	795	0.53	0.04710	7	0.0696	7.7	0.01071	3.2	68.7	±2.2
4.1	0.49	1131	663	0.61	0.05310	5.4	0.0921	7.2	0.01258	4.8	80.6	±3.9
5.1	0.30	2299	1297	0.58	0.04990	4.5	0.0782	4.7	0.01138	1.5	72.9	±1.1
6.1	0.24	1514	911	0.62	0.05010	2.9	0.0767	3.3	0.01110	1.5	71.2	±1.1
7.1	1.07	1656	905	0.56	0.04290	9.5	0.0619	11	0.01046	5.2	67.1	±3.5
8.1	0.42	1897	1173	0.64	0.05060	3	0.0890	4.4	0.01277	3.3	81.8	±2.7
9.1	0.23	1738	969	0.58	0.04890	2.8	0.0738	3.2	0.01095	1.6	70.2	±1.1
10.1	1.16	1758	966	0.57	0.04720	7	0.0755	7.1	0.01159	1.6	74.3	±1.2
11.1	1.43	1416	760	0.55	0.04520	8.6	0.0696	8.8	0.01116	1.7	71.6	±1.2
12.1	1.09	1857	1035	0.58	0.04690	7	0.0735	7.2	0.01137	1.8	72.9	±1.3
13.1	1.14	1504	808	0.56	0.04450	7	0.0677	7.3	0.01104	1.9	70.8	±1.4
14.1	2.35	1456	785	0.56	0.05010	10	0.0755	11	0.01093	2.8	70.1	±1.9
TCGY-11 (98°17′43″E, 25°20′56″N)												
1.1	0.00	3721	1927	0.54	0.05112	1.9	0.0833	8.1	0.01181	7.9	75.7	±5.9
2.1	0.18	2967	1046	0.36	0.04830	2.5	0.0878	8.3	0.01320	7.9	84.4	±6.6
3.1	0.59	2048	830	0.42	0.04860	4.5	0.1057	5.9	0.01577	3.7	100.9	±3.7
4.1	0.27	4063	1512	0.38	0.04779	2	0.0890	4.3	0.01351	3.8	86.5	±3.2
5.1	0.00	1631	911	0.58	0.05420	4.3	0.0862	6.5	0.01154	4.9	74.0	±3.6
6.1	2.47	526	462	0.91	0.04800	22	0.0690	23	0.01058	4	67.8	±2.7
7.1	0.24	2476	880	0.37	0.04810	2.5	0.0830	6.9	0.01253	6.4	80.3	±5.1
8.1	1.36	717	495	0.71	0.04750	8.4	0.0738	9.2	0.01127	3.8	72.3	±2.7
9.1	2.81	323	261	0.83	0.04450	14	0.0710	15	0.01151	4	73.8	±2.9
10.1	0.45	1543	391	0.26	0.04840	5.8	0.0778	6.9	0.01167	3.8	74.8	±2.8
11.1	0.57	1742	751	0.45	0.04940	4.3	0.0862	5.7	0.01265	3.7	81.1	±3.0
12.1	0.49	2496	773	0.32	0.04490	4	0.0806	7.4	0.01301	6.2	83.3	±5.2
13.1	1.53	865	919	1.10	0.04160	10	0.0681	11	0.01188	3.8	76.1	±2.9
14.1	0.44	1842	1273	0.71	0.04800	2.6	0.0765	4.5	0.01155	3.7	74.0	±2.7
15.1	0.51	1423	764	0.55	0.04700	6.1	0.0760	7.2	0.01174	3.8	75.2	±2.9
TCGY-3 (98°15′24″E, 25°18′34″N)												
1.1	0.54	1081	514	0.49	0.05940	3.5	0.0864	5.2	0.01056	3.8	67.7	±2.6
2.1	0.25	3385	1137	0.35	0.05090	2	0.0723	5.1	0.01030	4.6	66.1	±3.1
3.1	0.59	3307	1280	0.40	0.04820	5.1	0.0684	6.4	0.01030	3.9	66.0	±2.5
4.1	0.33	3649	1334	0.38	0.04700	4	0.0699	5.4	0.01080	3.7	69.2	±2.5
5.1	0.45	2126	1161	0.56	0.05070	2.9	0.0833	5.7	0.01192	5	76.4	±3.8
6.1	0.34	3458	1004	0.30	0.04640	3.9	0.0691	5.3	0.01082	3.7	69.4	±2.5
7.1	0.86	4239	1803	0.44	0.05180	3.1	0.0798	5	0.01116	3.9	71.6	±2.8
8.1	0.34	2768	1310	0.49	0.04850	2.7	0.0713	4.6	0.01067	3.7	68.4	±2.5
9.1	0.85	2847	922	0.33	0.04390	4.8	0.0639	6	0.01054	3.7	67.6	±2.5
10.1	0.25	1385	785	0.59	0.05090	2.9	0.0726	4.7	0.01035	3.8	66.4	±2.5
11.1	0.22	4402	2172	0.51	0.04980	2.1	0.0667	4.2	0.00972	3.7	62.4	±2.3
12.1	0.13	2481	1003	0.42	0.05300	2.2	0.0758	4.3	0.01038	3.7	66.6	±2.5
13.1	0.64	3010	969	0.33	0.04760	5.6	0.0714	6.7	0.01087	3.7	69.7	±2.6

(*continued on next page*)

Table 1 (*continued*)

Spot No.	$f^{206}Pb^*$	U (ppm)	Th (ppm)	$^{232}Th/^{238}U$	$^{207}Pb/^{206}Pb$	±% (1σ)	$^{207}Pb/^{235}U$	±% (1σ)	$^{206}Pb/^{238}U$ (1σ)	±% (Ma)	$^{206}Pb/^{238}U$ (Ma)	Age
TCLL-9 (98°15′HVE, 24°55′33″N)												
1.1	0.84	1995	1328	0.69	0.05250	7.7	0.0570	7.8	0.00787	1.7	50.6	±0.9
2.1	2.43	586	506	0.89	0.05210	13	0.0593	13	0.00824	2.3	52.9	±1.2
3.1	3.07	361	415	1.19	0.06000	18	0.0720	18	0.00869	2.7	55.8	±1.5
4.1	3.01	635	674	1.10	0.05440	12	0.0624	12	0.00831	2	53.4	±1.1
5.1	5.78	633	413	0.67	0.03600	36	0.0400	37	0.00818	2.6	52.5	±1.3
6.1	0.42	3741	1576	0.44	0.04680	3.2	0.0550	3.6	0.00851	1.7	54.6	±0.9
7.1	0.55	2291	1080	0.49	0.04830	6.3	0.0564	6.5	0.00846	1.5	54.3	±0.8
8.1	0.13	6574	1307	0.21	0.04770	2.4	0.0614	2.8	0.00935	1.4	60.0	±0.9
9.1	2.89	667	878	1.36	0.06430	14	0.0670	15	0.00757	4.8	48.6	±2.3
10.1	3.02	908	475	0.54	0.04190	21	0.0490	21	0.00850	2.3	54.6	±1.3
11.1	2.55	837	530	0.65	0.07110	11	0.0790	11	0.00806	2	51.8	±1.0
12.1	1.58	1397	1343	0.99	0.04840	8.6	0.0549	8.7	0.00823	1.7	52.8	±0.9
13.1	1.72	802	495	0.64	0.05340	9.8	0.0602	10	0.00817	2	52.5	±1.1
14.1	0.77	2227	1148	0.53	0.04810	4.4	0.0529	5	0.00798	2.4	51.2	±1.2
15.1	1.35	1179	596	0.52	0.04400	10	0.0498	10	0.00820	1.8	52.7	±1.0
LA-ICP-MS												
YJ-23 (′97°44′01″E, 24°iW37″N)						(2σ)		(2σ)		(2σ)		
1		1099	227	0.21	0.0492	1.6	0.0589	1.7	0.00868	1.3	55.7	±0.7
2		487	243	0.50	0.0480	2.0	0.0531	2.1	0.00803	1.2	51.6	±0.6
3		410	199	0.49	0.0481	2.2	0.0511	2.3	0.00771	1.3	49.5	±0.6
4		768	755	0.98	0.0527	1.9	0.0616	1.9	0.00849	1.3	54.5	±0.7
5		903	827	0.92	0.0527	2.4	0.0560	2.4	0.00772	1.3	49.6	±0.6
6		501	358	0.71	0.0476	2.3	0.0543	2.3	0.00827	1.2	53.1	±0.6
8		1115	737	0.66	0.0486	1.7	0.0527	1.8	0.00787	1.3	50.5	±0.6
9		704	307	0.44	0.0500	1.8	0.0571	1.9	0.00827	1.2	53.1	±0.6
11		155	127	0.82	0.0494	4.9	0.0534	4.8	0.00784	1.5	50.3	±0.8
12		443	263	0.59	0.0474	2.6	0.0516	2.6	0.00790	1.3	50.7	±0.6
13		117	61.4	0.52	0.0528	5.5	0.0585	5.4	0.00803	1.6	51.6	±0.8
14		441	123	0.28	0.0481	2.6	0.0549	2.6	0.00828	1.3	53.2	±0.7
15		594	168	0.28	0.0504	2.0	0.0571	2.0	0.00821	1.2	52.7	±0.6
16		253	196	0.77	0.0551	2.3	0.0634	2.4	0.00835	1.3	53.6	±0.7
17		517	578	1.12	0.0559	2.6	0.0584	2.6	0.00757	1.3	48.6	±0.6
18		306	203	0.66	0.0589	3.1	0.0632	3.0	0.00778	1.4	50.0	±0.7
19		327	180	0.55	0.0466	2.4	0.0540	2.4	0.00840	1.3	53.9	±0.7
20		63.6	37.9	0.60	0.0492	9.1	0.0594	8.9	0.00877	2.3	56.0	±1.0
21		920	483	0.52	0.0517	1.9	0.0588	2.0	0.00825	1.2	53.0	±0.6
22		552	331	0.60	0.0585	3.0	0.0659	3.0	0.00818	1.3	52.5	±0.7
23		1110	331	0.30	0.0519	1.8	0.0607	1.8	0.00848	1.2	54.4	±0.6
24		560	231	0.41	0.0519	3.4	0.0539	3.4	0.00752	1.3	48.3	±0.6
25		448	262	0.59	0.0509	2.3	0.0567	2.3	0.00808	1.2	51.9	±0.6
26		2398	5732	2.39	0.0496	1.6	0.0590	1.6	0.00863	1.3	55.4	±0.7
28		429	215	0.50	0.0771	2.4	0.0910	2.4	0.00857	1.3	55.0	±0.7
29		454	382	0.84	0.0486	2.2	0.0563	2.2	0.00841	1.3	54.0	±0.7
30		341	227	0.67	0.1148	2.8	0.1494	2.7	0.00944	1.5	60.6	±0.9
LD-1 (97°51′45″E, 24°58′14″N)												
1		224	197	1.14	0.06076	22.3	0.07325	20.1	0.0087	10.0	56	6
2		280	351	0.80	0.07551	3.9	0.08773	3.4	0.00838	2.6	53	2
3		219	230	0.95	0.10432	4.4	0.12638	3.7	0.00874	3.1	54	2
4		283	358	0.79	0.07613	5.0	0.10007	4.4	0.00948	3.1	60	2
5		163	169	0.96	0.12876	5.3	0.17678	4.3	0.00991	3.6	58	3
6		261	253	1.03	0.14057	4.3	0.19085	3.4	0.0098	3.2	58	2
7		63	91	0.70	0.19871	6.8	0.28217	5.0	0.01025	5.0	55	3
8		239	287	0.83	0.13831	4.8	0.177	3.8	0.00924	3.5	54	2
9		340	492	0.69	0.06331	4.8	0.07507	4.3	0.00856	2.8	54	2
10		288	411	0.70	0.07654	4.0	0.09581	3.4	0.00904	2.7	57	2
11		201	272	0.74	0.09121	5.9	0.11816	5.0	0.00935	3.5	58	2
12		132	139	0.95	0.08363	18.9	0.10821	16.2	0.00934	10.1	60	6
13		351	341	1.03	0.08076	5.3	0.0963	4.6	0.00861	3.3	54	2
14		186	296	0.63	0.07792	4.7	0.11181	4.1	0.01036	2.9	65	2
15		313	314	1.00	0.08336	5.3	0.10529	4.7	0.00912	3.1	57	2
15		388	464	0.84	0.07306	4.4	0.09181	3.8	0.00907	2.8	57	2
16		308	377	0.82	0.12414	3.9	0.16348	3.1	0.00951	2.9	57	2
17		309	553	0.56	0.09429	3.6	0.11634	3.0	0.00891	2.6	55	2
18		63	112	0.56	0.15761	9.3	0.20081	7.1	0.0092	6.3	51	3
19		252	244	1.03	0.09859	6.6	0.12339	5.6	0.00904	4.0	55	3
20		894	597	1.50	0.0655	3.6	0.07784	3.2	0.00858	2.4	55	1
21		548	422	1.30	0.07249	4.8	0.0908	4.2	0.00905	3.0	58	2
22		188	226	0.83	0.05934	10.1	0.07302	9.0	0.00889	4.9	57	3
23		266	298	0.90	0.07274	5.5	0.09015	4.8	0.00895	3.2	57	2
24		187	221	0.85	0.10459	8.2	0.13508	6.8	0.00933	5.0	56	3
25		513	254	2.02	0.05789	9.8	0.07072	8.8	0.00882	4.8	57	3

Table 1 *(continued)*

CBZ-4 (97°45′12″E, 25°01′10″N)										
1	194	226	0.86	0.08597	4.5	0.13202	3.8	0.01113	2.5	69	2
2	205	226	0.91	0.13643	3.8	0.21299	3.1	0.01132	2.5	68	2
3	119	180	0.66	0.22887	3.9	0.42444	2.9	0.01345	2.8	68	3
4	452	704	0.64	0.08484	2.9	0.12766	2.5	0.01091	1.7	67	1
5	174	238	0.73	0.07882	4.7	0.11269	4.2	0.01037	2.5	65	2
6	85	144	0.59	0.11243	5.8	0.17764	5.0	0.01146	3.2	68	2
7	213	344	0.62	0.07561	3.4	0.1085	3.0	0.0104	1.9	65	1
8	574	1248	0.46	0.05494	2.3	0.07528	2.0	0.00993	1.3	63.4	0.9
9	133	130	1.02	0.1429	4.7	0.22942	3.8	0.01164	3.0	69	2
10	133	200	0.66	0.1242	4.0	0.20138	3.3	0.01176	2.5	69	2
11	161	234	0.69	0.08306	5.0	0.12575	4.3	0.01098	2.7	68	2
12	554	814	0.68	0.05103	3.0	0.07563	2.7	0.01074	1.6	69	1
13	192	267	0.72	0.10754	4.1	0.15706	3.4	0.01059	2.4	63	2
14	110	153	0.72	0.10157	5.7	0.15317	4.9	0.01093	3.2	66	2
15	165	232	0.71	0.07689	4.8	0.11163	4.2	0.01052	2.6	65	2
16	840	1741	0.48	0.05362	3.2	0.08448	2.9	0.01142	1.7	73	1
17	208	254	0.82	0.08559	4.3	0.12106	3.7	0.01025	2.3	63	2
18	428	487	0.88	0.07564	3.3	0.10907	2.9	0.01045	1.8	66	1
19	1072	2681	0.40	0.06156	1.9	0.08622	1.7	0.01015	1.3	64.1	0.8
20	153	339	0.45	0.20725	4.4	0.33527	3.3	0.01172	3.2	60	2
21	335	782	0.43	0.05672	2.7	0.08329	2.4	0.01064	1.5	68	1
22	79	179	0.44	0.12836	7.6	0.17102	6.1	0.00966	4.6	56	2
23	192	388	0.50	0.06116	4.0	0.08442	3.6	0.01	2.0	63	1
24	183	246	0.75	0.09061	4.1	0.13682	3.5	0.01094	2.3	67	2
25	135	234	0.58	0.06152	5.2	0.09246	4.7	0.01089	2.5	69	2
CBZ-6 (97°45′12″E, 25°01′10″N)											
1	282	1201	0.24	0.04693	1.4	0.06841	1.3	0.01056	1.1	67.7	0.8
2	1154	832	1.39	0.04839	3.0	0.07079	2.7	0.0106	1.5	68	1
3	282	2588	0.11	0.04916	1.1	0.06784	1.0	0.01	1.0	64.1	0.6
4	326	768	0.42	0.05214	2.0	0.0803	1.8	0.01116	1.3	71.5	0.9
5	95	308	0.31	0.05407	6.2	0.10008	5.8	0.01341	2.5	85	2
6	652	485	1.34	0.06078	4.2	0.08968	3.8	0.01069	2.1	69	1
7	480	1911	0.25	0.05482	0.9	0.08309	0.9	0.01098	1.0	70	0.7
8	277	174	1.59	0.05811	9.4	0.111	8.5	0.01384	4.3	89	4
9	372	1001	0.37	0.05696	1.0	0.09682	0.9	0.01231	1.1	78.7	0.8
10	98	131	0.75	0.09853	1.2	2.32184	1.0	0.17071	1.2	984	12
11	334	336	0.99	0.05248	6.1	0.07573	5.5	0.01045	2.7	67	2
12	2728	7638	0.36	0.04685	0.6	0.06698	0.6	0.01036	1.0	66.4	0.6
13	224	1635	0.14	0.05429	1.3	0.11964	1.1	0.01596	1.1	102	1
14	510	1936	0.26	0.0514	0.9	0.07712	0.9	0.01087	1.0	69.7	0.7
15	364	1315	0.28	0.0526	1.1	0.08415	1.0	0.01159	1.0	74.3	0.8
16	426	333	1.28	0.06186	3.8	0.10007	3.4	0.01171	2.0	75	1
17	1616	4444	0.36	0.0482	1.0	0.07097	0.9	0.01066	1.0	68.4	0.7
18	242	633	0.38	0.05695	3.1	0.08586	2.8	0.01092	1.6	70	1
19	2726	1559	1.75	0.06187	1.1	0.09452	1.0	0.01106	1.1	70.9	0.8
20	446	577	0.77	0.05145	2.3	0.18475	2.1	0.026	1.3	165	2
21	196	817	0.24	0.06128	3.7	0.09882	3.4	0.01168	1.8	74	1
22	646	2799	0.23	0.16924	3.4	0.27868	2.7	0.01192	2.3	72	2
23	940	815	1.15	0.08542	1.9	0.13204	1.7	0.01119	1.3	71	1
NB07-18 (97°34′59″E, 24°36′42″N)											
1	764	1708	0.45	0.05384	4.3	0.06084	3.9	0.0082	2.6	53	1
2	961	1552	0.62	0.05914	2.1	0.06933	1.9	0.0085	2.0	54	1
3	658	960	0.69	0.05627	30.3	0.06827	27.8	0.0088	12.4	56	7
4	800	1385	0.58	0.05604	2.3	0.06405	2.1	0.00829	2.1	53	1
5	524	1114	0.45	0.06193	2.5	0.07053	2.2	0.00826	2.2	53	1
6	734	2073	0.35	0.05782	2.0	0.06588	1.8	0.00826	2.1	53	1
7	692	1457	0.48	0.05316	2.8	0.06179	2.6	0.00843	2.1	54	1
8	1618	2623	0.62	0.05239	2.6	0.06179	2.4	0.00855	2.1	55	1
9	367	963	0.38	0.05789	2.9	0.07025	2.6	0.0088	2.3	56	1
10	846	965	0.88	0.07411	3.8	0.08895	3.4	0.0087	2.6	55	2
11	832	1681	0.49	0.055	2.3	0.064	2.1	0.00844	2.1	54	1
12	335	821	0.41	0.08278	3.9	0.09792	3.4	0.00858	2.7	53	1
13	194	1069	0.18	0.06034	5.4	0.06969	4.9	0.00837	3.0	53	2
14	659	1390	0.47	0.08787	3.0	0.10496	2.6	0.00866	2.4	54	1
15	2098	2377	0.88	0.05721	3.3	0.06712	3.0	0.00851	2.4	55	1
16	222	413	0.54	0.10055	5.9	0.11977	5.0	0.00864	3.7	52	2
17	1497	3234	0.46	0.05953	1.8	0.07304	1.7	0.0089	2.0	57	1
18	533	1006	0.53	0.07179	6.3	0.08725	5.5	0.00881	3.5	56	2
19	513	867	0.59	0.07311	4.2	0.0889	3.7	0.00881	2.7	55	2
20	423	913	0.46	0.06064	6.0	0.07425	5.4	0.00888	3.3	56	2
21	477	813	0.59	0.07064	3.5	0.08229	3.2	0.00845	2.5	53	1
22	460	1253	0.37	0.06063	2.8	0.0704	2.5	0.00842	2.1	53	1
23	194	1144	0.17	0.07305	2.4	0.08464	2.2	0.0084	2.1	52	1
24	184	968	0.19	0.05703	2.6	0.06367	2.4	0.00809	2.1	51	1
25	286	708	0.40	0.0736	2.9	0.08486	2.5	0.00836	2.3	52	1

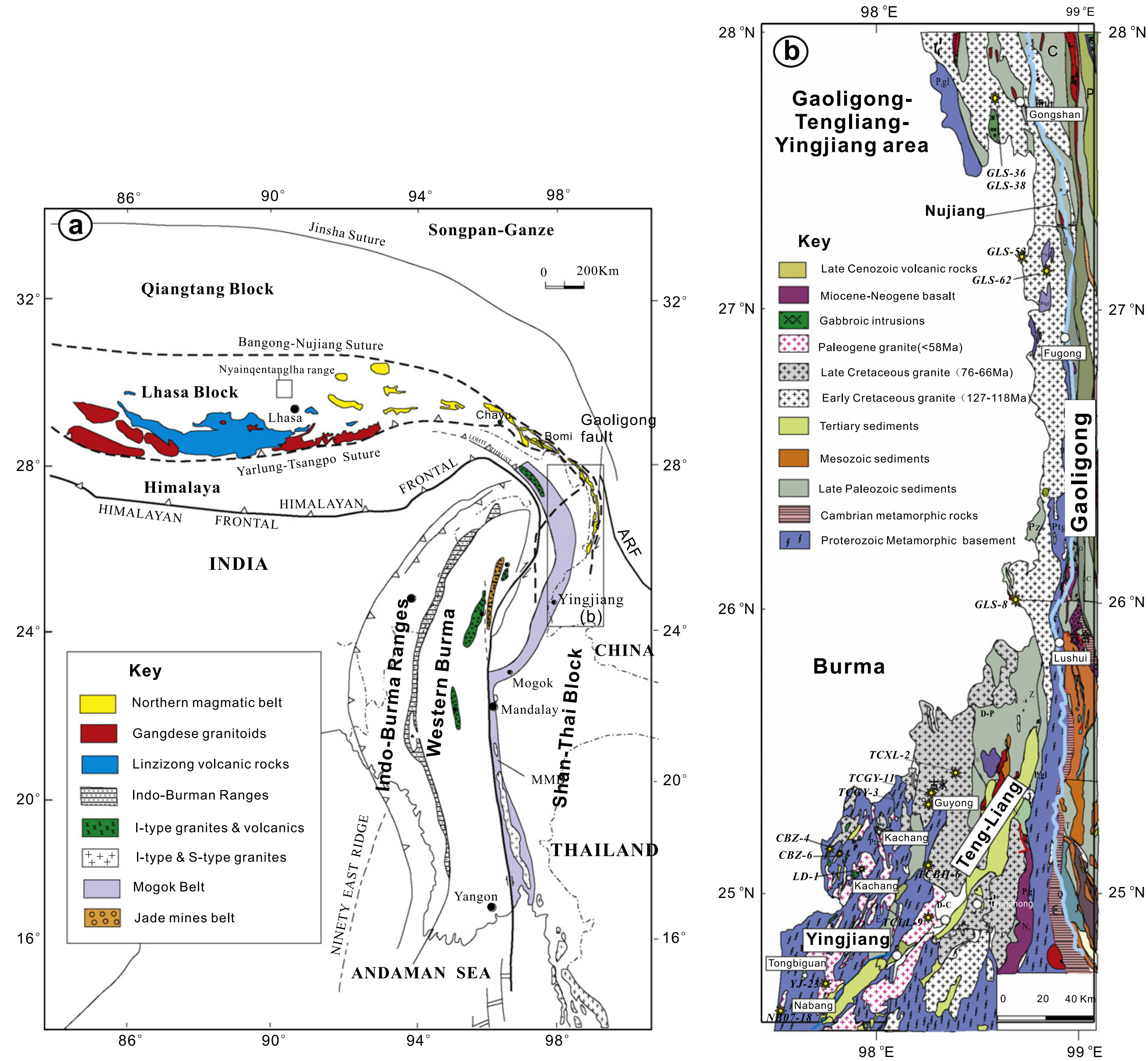

Fig. 1. (a) Generalized tectonic map of the Tibetan Plateau and SE Asia (modified after Chung et al. (2005) and Mitchell (1993)). (b) Simplified geologic map of the Gaoligong–Tengliang–Yingjiang (GTY) area showing sample localities and major geologic units (modified after Pan et al. (2004)).

these magmatic rocks and elucidating their genesis are therefore pivotal for deciphering tectonic history, including rifting, shearing event and closure of Meso-Tethyan and Neo-Tethyan oceans and collision between different blocks that amalgamated (Scharer et al., 1984; Xu et al., 1985; Coulon et al., 1986; Pearce and Mei, 1988; Turner et al., 1996; Ding et al., 2003; Booth et al., 2004; Xu et al., 2008; Chung et al., 2005; Wen et al., 2008; Chiu et al., 2009; Ji et al., 2009; Zhu et al., 2009).

Much data are now available for post-collisional magmatism in the Lhasa Terrane, in the frontal collisional belt (Fig. 1a). Comparatively, pre- and syn-collisional magmatism, especially in eastern Tibet and western Yunnan is still poorly characterized. For this reason, the Gaoligong–Tengliang–Yingjiang (abbreviated as GTY) belt in western Yunnan, a major intracontinental dextral strike-slip fault which possibly accommodates the extrusion of the Tibetan plateau (Wang et al., 2006), is targeted for this study. The GPS data clearly illustrate the eastward motion of the Tibetan Plateau and that it turns south along the Eastern Himalayan Syntaxis (Chen et al., 2000; Wang et al., 2001). This leads to the speculation that the GTY belt may represent the rotated, eastward extension of the Lhasa terrane. To test this idea, we performed bulk rock chemistry, SHRIMP and ICP-MS U–Pb dating and in situ LA-MC-ICPMS Hf isotope analyses on zircons extracted from granitoids from the GTY belt, east of the eastern Himalayan Syntaxis. The data are compared with those available for the Lhasa terrane and for Southeast Asian (Burma, Thailand and Malaysia) in order to unravel the similarity and difference in pre- and syn-collisional magmatism in the two regions. We are particularly concerned with the relative contribution of mantle and crust in magma genesis, which can be used to understand the behavior of deep crust and mantle during the evolution of the Tibetan Plateau and to constrain tectonic setting of the associated magmatism.

2. Geologic setting and tectonic background

The Tibetan Plateau is composed of a number of diverse exotic blocks that were accreted at different time. These blocks, namely

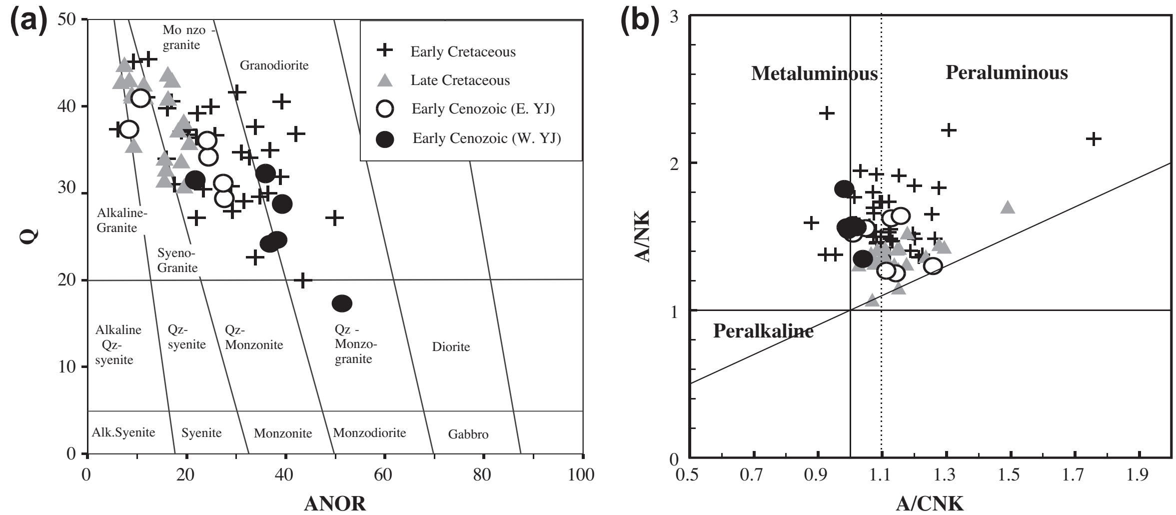

Fig. 2. (a) Q′-ANOR classification diagram (Streckeisen and Le Maitre, 1979) for the Gaoligong and Tengliang granites; ANOR = An/(Or + An) × 100; Q′ = Q/(Q + Or + Ab + An) × 100; (b) ANK vs. A/CNK plot showing the peraluminous to strongly peraluminous nature of the Gaoligong–Tengliang granites, and metaluminous feature of the Yingjiang samples; A = Al_2O_3, N = Na_2O, K = K_2O, C = CaO (all in molar proportion).

India, Lhasa and Qiangtang, are separated by different sutures (Fig. 1a). The Yarlung–Tsangpo suture separated the Indian plate and Lhasa block. The latter is separated from the Qiangtang Terrane by the Bangong-Nujiang suture zone. The ages of these successive sutures decrease from north to south. For instance, the closure of the Meso-Tethys (leading to the Bangong-Nujiang suture) took place during the late Jurassic and early Cretaceous (Yin and Nie, 1996; Yin and Harrison, 2000; Kapp et al., 2005b), and the closure of the Neo-Tethys (leading to the Yarlung–Tsangpo suture) happened after the late Cretaceous. In fact, the initiation age of the India–Asia collision remains a matter of considerable debate, with views ranging from Late Cretaceous (>65 Ma) to as young as Oligocene (34 Ma) (Searle et al., 1987; Rowley, 1996; Yin and Harrison, 2000; Aitchison et al., 2007). The currently popular view is that this event took place at ca. 55 Ma (see review of Wu et al., 2008). Two magmatic suites have been identified in the Lhasa terrane, namely the southern Gangdese belt and the northern magmatic belt (Coulon et al., 1986; Chung et al., 2005; Chu et al., 2006; Wen et al., 2008). The Gangdese belt, a huge quasi-continuous 2600 km long and 100 km wide belt, is composed of the Jurassic, and predominant late Cretaceous to Paleogene batholith ranging from gabbro to granite (Debon et al., 1985; Wen et al., 2008). The northern magmatic belt is dominated by Jurassic–Early Cretaceous peraluminous or S-type granitic plutons (Xu et al., 1985; Lee et al., 2003; Chu et al., 2006).

The area covered by the north–south trending Gaoligong belt is situated to east of the eastern Himalayan Syntaxis (Fig. 1b). This mountain range is 3000 m high and marks the divide between the Longchuanjiang in the west and the Nujiang (Salween) in the east. The core of the Gaoligong range is composed of Precambrian high-grade metamorphic, late Paleozoic clastic rocks and carbonates, and granitic intrusives. They are intensely deformed and affected by a sub-vertical foliation, dipping toward both east and west directions. Ductile shear sense criteria show a right-lateral motion (Fig. 1b). The mylonitization is dated between 10 and 18 Ma (Zhong et al., 1999; Yang QJ et al., unpublished data), in agreement with the dextral shearing along the Jiali fault and Karakorum fault (Lee et al., 2003; Searle, 1996).

The N–S-trending Gaoligong fault extends south-westward into the Tengchong–Lianghe–Yingjiang area, and likely extends further into the Shan Scarp in Burma (Fig. 1a). The basement in the GTY area is also composed of flat foliated granites and metamorphic rocks. The NNE-trending granites are less deformed compared to the Gaoligong granites. Late Cenozoic volcanic eruption took place in the Tengchong and Yingjiang area (Zhu et al., 1983; Chen et al., 2002). This, together with widespread thermal activity, marks the tectonically active nature of the region. The Yingjiang area, east of the China–Burma border, probably represents the northern extension of the Mogok metamorphic belt (Fig. 1a).

Given the tectonic position of the studied area and the purpose of this study, a brief introduction to Burman geology is necessary. Burma occupied a complex tectonic zone extending from the northern continuation of the active Sunda–Andaman arc into the eastern Himalayan syntaxis. Geologically, Burma includes three parts, namely, the Indo–Burman Range accretionary prism, Burma microplate and eastern Burma Highlands that represent the westernmost extent of Sundaland (Fig. 1a). The latter two are separated by the right lateral strike-slip Sagaing fault that accommodates some of the northward motion of the India subsequent to the collision (Searle et al., 2007). The western edge of the Burma plate is bounded by the Indo–Burma Range, which is interpreted as accretionary prism generated by the eastward subduction of the Indian oceanic plate (Mitchell, 1993). The Burma microplate was probably continuous northward to the Lhasa block, which formed the southern margin of the Asian plate with semicontinuous Gangdese magmatism from Jurassic to Paleogene time (Chung et al., 2005; Chu et al., 2006). Similar calc-alkaline magmatism in Burma extends as far back as the Middle Jurassic (Mitchell, 1993; Barley et al., 2003). Recent geochronologic study reported zircon ages of Jurassic, mid-Cretaceous and early Eocene time, confirming that Andean-type granite magmatism was widespread along the Burma margin throughout the precollisional period. This Andean, I-type magmatism may have resulted from subduction of Tethyan oceanic lithosphere beneath the southern margin of the Asian continents prior to the Indo–Asian collision.

A string of ultramafic rocks of Early Cretaceous–Eocene age containing high-pressure metamorphic facies run along and adjacent to the trend of the Sagaing Fault (Mitchell, 1993; Hughes et al., 2000). These rocks are interpreted as ophiolite marking the collision zone of the Burma microplate and the Shan-Thai block, generating a belt of S-type granite (i.e., the western belt, Cobbing et al., 1986; Zaw, 1990) running from south of Mandalay southwards through the Shan Scarps and southwestern Burma into

Table 2
Zircon Hf isotopes for the granitic batholiths from Gaoligong, Tengliang and Yingjiang.

Sample spot	$^{176}Yb/^{177}Hf$	$^{176}Lu/^{177}Hf$	$^{176}Hf/^{177}Hf$	2σ	$^{206}Pb/^{235}U$ age (Ma)	$^{176}Hf/^{177}Hf$ (t)	ε_{Hf} (t)	T_{dm} (Ga)
GLS-36								
1	0.015675	0.000599	0.282395	0.000022	118	0.282394	−10.78	1.20
2	0.025306	0.001043	0.282455	0.000020	124	0.282452	−8.59	1.13
3	0.021614	0.000941	0.282460	0.000023	124	0.282458	−8.40	1.12
4	0.024399	0.001079	0.282469	0.000021	124	0.282466	−8.09	1.11
5	0.025041	0.001137	0.282470	0.000025	124	0.282467	−8.07	1.11
6	0.031161	0.001365	0.282470	0.000020	125	0.282467	−8.05	1.12
7	0.021267	0.000898	0.282470	0.000021	121	0.282468	−8.09	1.10
8	0.018195	0.000731	0.282470	0.000021	118	0.282469	−8.13	1.10
9	0.014477	0.000588	0.282471	0.000023	117	0.282470	−8.14	1.09
10	0.019690	0.000830	0.282472	0.000021	127	0.282470	−7.90	1.10
11	0.035614	0.001447	0.282482	0.000022	125	0.282479	−7.63	1.10
12	0.032860	0.001396	0.282494	0.000026	128	0.282491	−7.15	1.08
13	0.032785	0.001466	0.282498	0.000030	127	0.282495	−7.03	1.08
14	0.035395	0.001302	0.282503	0.000018	128	0.282499	−6.84	1.07
15	0.021770	0.000923	0.282506	0.000022	130	0.282503	−6.66	1.05
16	0.026519	0.001083	0.282506	0.000029	129	0.282503	−6.66	1.06
17	0.048011	0.002123	0.282552	0.000042	129	0.282547	−5.14	1.02
GLS-38								
1	0.013316	0.000560	0.282200	0.000020	126	0.282199	−17.52	1.47
2	0.051207	0.002170	0.282364	0.000028	126	0.282359	−11.83	1.29
3	0.022997	0.001000	0.282443	0.000023	126	0.282441	−8.95	1.14
4	0.027945	0.001214	0.282450	0.000024	126	0.282447	−8.72	1.14
5	0.029372	0.001247	0.282455	0.000023	126	0.282452	−8.56	1.13
6	0.027149	0.001178	0.282467	0.000025	126	0.282464	−8.12	1.11
7	0.023849	0.001103	0.282470	0.000021	126	0.282468	−8.00	1.11
8	0.030238	0.001289	0.282471	0.000019	126	0.282468	−7.98	1.11
9	0.023869	0.001066	0.282472	0.000025	126	0.282469	−7.94	1.10
10	0.021232	0.000928	0.282474	0.000022	126	0.282472	−7.85	1.10
11	0.020790	0.000926	0.282475	0.000025	126	0.282473	−7.82	1.10
12	0.024961	0.001115	0.282481	0.000026	126	0.282479	−7.61	1.09
13	0.024640	0.001086	0.282487	0.000022	126	0.282485	−7.40	1.08
14	0.022878	0.000982	0.282488	0.000025	126	0.282486	−7.35	1.08
15	0.033257	0.001459	0.282495	0.000024	126	0.282491	−7.16	1.08
16	0.028579	0.001101	0.282536	0.000029	126	0.282533	−5.67	1.02
17	0.026456	0.001196	0.282547	0.000026	126	0.282544	−5.30	1.00
18	0.025300	0.001119	0.282623	0.000058	126	0.282621	−2.59	0.89
GLS-8								
1	0.028502	0.001032	0.282165	0.000018	122	0.282163	−18.87	1.53
2	0.030564	0.001250	0.282366	0.000026	117	0.282363	−11.89	1.26
3	0.024353	0.001040	0.282392	0.000020	122	0.282390	−10.83	1.22
4	0.035220	0.001257	0.282395	0.000025	121	0.282392	−10.78	1.22
5	0.019659	0.000764	0.282433	0.000022	125	0.282432	−9.30	1.15
6	0.028980	0.001093	0.282451	0.000019	122	0.282448	−8.78	1.14
7	0.023654	0.000909	0.282487	0.000028	122	0.282485	−7.48	1.08
8	0.026163	0.001036	0.282501	0.000025	123	0.282499	−6.96	1.06
9	0.028056	0.001194	0.282510	0.000020	125	0.282507	−6.63	1.06
10	0.028574	0.001055	0.282513	0.000025	122	0.282510	−6.57	1.05
11	0.030757	0.001251	0.282520	0.000020	122	0.282517	−6.35	1.04
12	0.032711	0.001372	0.282520	0.000018	122	0.282517	−6.34	1.05
13	0.037176	0.001366	0.282522	0.000022	125	0.282519	−6.23	1.04
14	0.053182	0.002015	0.282523	0.000022	122	0.282518	−6.29	1.06
15	0.033750	0.001291	0.282525	0.000024	117	0.282522	−6.27	1.04
16	0.033779	0.001291	0.282526	0.000024	120	0.282523	−6.17	1.04
17	0.026455	0.001143	0.282543	0.000058	122	0.282540	−5.52	1.01
18	0.030269	0.001290	0.282548	0.000020	122	0.282545	−5.33	1.00
19	0.022290	0.000868	0.282555	0.000048	157	0.282552	−4.32	0.98
20	0.082753	0.002890	0.282564	0.000026	122	0.282557	−4.91	1.02
GLS-62								
1	0.031205	0.000952	0.282550	0.000030	118	0.282548	−5.35	0.99
2	0.035857	0.001198	0.282574	0.000026	121	0.282571	−4.44	0.96
3	0.034811	0.001059	0.282578	0.000029	116	0.282576	−4.38	0.95
4	0.028987	0.000943	0.282583	0.000034	117	0.282581	−4.18	0.95
5	0.031729	0.001077	0.282587	0.000022	118	0.282584	−4.05	0.94
6	0.030001	0.001051	0.282596	0.000021	126	0.282593	−3.55	0.93
7	0.105017	0.003701	0.282596	0.000057	118	0.282588	−3.93	1.00
8	0.042222	0.001504	0.282603	0.000024	111	0.282600	−3.66	0.93
9	0.047781	0.001394	0.282605	0.000029	109	0.282602	−3.61	0.93
10	0.053938	0.002193	0.282606	0.000022	118	0.282601	−3.46	0.94
11	0.033418	0.001173	0.282613	0.000025	136	0.282610	−2.76	0.91
12	0.044050	0.001433	0.282613	0.000025	116	0.282610	−3.18	0.91
13	0.039492	0.001376	0.282618	0.000025	133	0.282615	−2.64	0.91
14	0.050639	0.001618	0.282625	0.000025	125	0.282621	−2.60	0.90

Table 2 (*continued*)

Sample spot	$^{176}Yb/^{177}Hf$	$^{176}Lu/^{177}Hf$	$^{176}Hf/^{177}Hf$	2σ	$^{206}Pb/^{235}U$ age (Ma)	$^{176}Hf/^{177}Hf$ (t)	ε_{Hf} (t)	T_{dm} (Ga)
15	0.044847	0.001530	0.282629	0.000020	126	0.282626	−2.42	0.89
16	0.099861	0.003652	0.282652	0.000046	112	0.282644	−2.07	0.91
17	0.104925	0.003786	0.282653	0.000030	118	0.282644	−1.93	0.92
18	0.081210	0.002695	0.282721	0.000027	118	0.282715	0.59	0.79
19	0.104875	0.003467	0.282729	0.000053	118	0.282721	0.79	0.79
20	0.123518	0.003818	0.282761	0.000020	118	0.282752	1.90	0.75
GLS-53								
1	0.038684	0.001571	0.282470	0.000040	84	0.282468	−8.93	1.12
2	0.038868	0.001504	0.282484	0.000021	81	0.282482	−8.50	1.10
3	0.028743	0.001159	0.282490	0.000017	66	0.282489	−8.57	1.08
4	0.053833	0.002124	0.282491	0.000033	73	0.282488	−8.44	1.11
5	0.033173	0.001280	0.282494	0.000087	79	0.282492	−8.17	1.08
6	0.030158	0.001208	0.282498	0.000024	76	0.282497	−8.07	1.07
7	0.031437	0.001278	0.282508	0.000019	64	0.282507	−7.99	1.06
8	0.035002	0.001415	0.282510	0.000021	72	0.282508	−7.74	1.06
9	0.032555	0.001306	0.282511	0.000037	76	0.282509	−7.62	1.06
10	0.025392	0.001018	0.282521	0.000021	76	0.282520	−7.26	1.03
11	0.065622	0.002362	0.282524	0.000046	76	0.282520	−7.23	1.07
12	0.032810	0.001336	0.282527	0.000020	80	0.282525	−6.99	1.04
13	0.045014	0.001774	0.282530	0.000020	76	0.282527	−6.99	1.04
14	0.039700	0.001517	0.282547	0.000020	69	0.282545	−6.54	1.01
15	0.051506	0.002014	0.282558	0.000045	76	0.282555	−6.00	1.01
16	0.042722	0.001572	0.282569	0.000039	76	0.282566	−5.61	0.98
17	0.066984	0.002259	0.282572	0.000063	76	0.282569	−5.51	0.99
18	0.034967	0.001385	0.282574	0.000017	75	0.282572	−5.42	0.97
19	0.035463	0.001418	0.282578	0.000048	73	0.282576	−5.34	0.96
TCGY-3								
1	0.061625	0.002385	0.282363	0.000021	68	0.282360	−13.07	1.30
2	0.089261	0.003675	0.282369	0.000025	68	0.282365	−12.91	1.34
3	0.032107	0.001403	0.282373	0.000024	66	0.282371	−12.74	1.26
4	0.042972	0.001789	0.282373	0.000019	68	0.282371	−12.71	1.27
5	0.050761	0.002142	0.282373	0.000024	69	0.282371	−12.68	1.28
6	0.042813	0.001817	0.282386	0.000039	68	0.282384	−12.24	1.25
7	0.031426	0.001362	0.282392	0.000033	76	0.282391	−11.83	1.23
8	0.089480	0.003719	0.282393	0.000021	72	0.282388	−12.00	1.31
9	0.053984	0.002317	0.282397	0.000017	70	0.282394	−11.84	1.25
10	0.055602	0.002329	0.282397	0.000024	62	0.282394	−12.00	1.25
11	0.058854	0.002401	0.282399	0.000021	68	0.282396	−11.82	1.25
12	0.041481	0.001781	0.282399	0.000020	69	0.282397	−11.76	1.23
13	0.038598	0.001607	0.282401	0.000034	68	0.282399	−11.69	1.22
14	0.072440	0.003050	0.282414	0.000021	68	0.282410	−11.31	1.25
15	0.066976	0.002823	0.282435	0.000034	67	0.282432	−10.58	1.21
16	0.062379	0.002603	0.282445	0.000028	66	0.282442	−10.22	1.19
17	0.036882	0.001601	0.282486	0.000029	66	0.282484	−8.73	1.10
TCGY-11								
1	0.023820	0.000700	0.282469	0.000036	74	0.282468	−9.15	1.10
2	0.032739	0.000938	0.282472	0.000033	81	0.282471	−8.88	1.10
3	0.035179	0.001018	0.282497	0.000038	80	0.282496	−8.01	1.07
4	0.026272	0.000708	0.282497	0.000032	75	0.282496	−8.11	1.06
5	0.033018	0.000932	0.282504	0.000036	74	0.282503	−7.89	1.06
6	0.043729	0.001273	0.282516	0.000030	84	0.282514	−7.29	1.05
7	0.042312	0.001131	0.282519	0.000045	76	0.282517	−7.36	1.04
8	0.040473	0.001416	0.282520	0.000026	74	0.282518	−7.37	1.05
9	0.044562	0.001290	0.282528	0.000028	87	0.282526	−6.80	1.03
10	0.033589	0.000916	0.282529	0.000032	72	0.282528	−7.04	1.02
11	0.037235	0.001095	0.282536	0.000030	101	0.282534	−6.22	1.02
12	0.047030	0.001415	0.282551	0.000028	83	0.282549	−6.06	1.00
13	0.033835	0.001024	0.282570	0.000028	68	0.282568	−5.71	0.97
14	0.060902	0.001761	0.282597	0.000031	76	0.282594	−4.61	0.95
TCBH-6								
1	0.040824	0.001578	0.282389	0.000031	81	0.282386	−11.87	1.24
2	0.033382	0.001231	0.282408	0.000032	69	0.282406	−11.43	1.20
3	0.042622	0.001681	0.282416	0.000024	72	0.282414	−11.08	1.20
4	0.039910	0.001568	0.282425	0.000021	72	0.282423	−10.79	1.19
5	0.032458	0.001261	0.282425	0.000027	73	0.282423	−10.74	1.18
6	0.048913	0.001921	0.282426	0.000025	71	0.282423	−10.78	1.20
7	0.024529	0.000920	0.282429	0.000020	73	0.282428	−10.59	1.16
8	0.028496	0.001125	0.282430	0.000025	74	0.282428	−10.53	1.17
9	0.055648	0.002157	0.282433	0.000022	70	0.282430	−10.55	1.19
10	0.037222	0.001470	0.282434	0.000022	73	0.282432	−10.44	1.17
11	0.027024	0.001028	0.282436	0.000032	67	0.282435	−10.45	1.15
12	0.030564	0.001162	0.282437	0.000027	70	0.282435	−10.38	1.16
13	0.035710	0.001395	0.282439	0.000026	82	0.282436	−10.07	1.16

(*continued on next page*)

Table 2 (*continued*)

Sample spot	$^{176}Yb/^{177}Hf$	$^{176}Lu/^{177}Hf$	$^{176}Hf/^{177}Hf$	2σ	$^{206}Pb/^{235}U$ age (Ma)	$^{176}Hf/^{177}Hf$ (t)	ε_{Hf} (t)	T_{dm} (Ga)
14	0.039530	0.001500	0.282442	0.000024	77	0.282440	−10.07	1.16
15	0.064908	0.002538	0.282445	0.000019	72	0.282441	−10.12	1.19
16	0.044639	0.001737	0.282450	0.000025	72	0.282448	−9.88	1.16
17	0.048835	0.001944	0.282489	0.000019	72	0.282487	−8.51	1.11
18	0.064026	0.001892	0.282502	0.000039	71	0.282499	−8.09	1.09
TCXL-2								
1	0.030166	0.001165	0.282441	0.000034	76	0.282440	−10.08	1.15
2	0.023760	0.000897	0.282452	0.000060	76	0.282450	−9.71	1.13
3	0.046913	0.001783	0.282462	0.000023	76	0.282459	−9.39	1.14
4	0.028161	0.001122	0.282466	0.000024	76	0.282464	−9.22	1.12
5	0.021902	0.000853	0.282470	0.000025	76	0.282469	−9.04	1.10
6	0.032882	0.001325	0.282477	0.000022	76	0.282476	−8.82	1.10
7	0.034666	0.001516	0.282484	0.000025	76	0.282482	−8.58	1.10
8	0.044135	0.001676	0.282492	0.000027	76	0.282490	−8.31	1.09
9	0.064465	0.002407	0.282508	0.000026	76	0.282504	−7.81	1.09
10	0.053687	0.002070	0.282519	0.000034	76	0.282516	−7.39	1.07
11	0.055168	0.002077	0.282519	0.000028	76	0.282516	−7.39	1.07
12	0.055582	0.002128	0.282525	0.000044	76	0.282522	−7.17	1.06
13	0.071165	0.002701	0.282530	0.000026	76	0.282526	−7.04	1.07
14	0.028287	0.001060	0.282532	0.000024	76	0.282531	−6.87	1.02
15	0.048297	0.001835	0.282539	0.000038	76	0.282536	−6.67	1.03
16	0.081422	0.003148	0.282558	0.000031	76	0.282554	−6.05	1.04
17	0.079018	0.002990	0.282566	0.000031	76	0.282562	−5.76	1.02
TCLL-9								
1	0.024330	0.001039	0.282392	0.000020	53	0.282391	−12.30	1.22
2	0.023173	0.000905	0.282447	0.000022	53	0.282446	−10.38	1.14
3	0.033604	0.001333	0.282453	0.000024	54	0.282452	−10.15	1.14
4	0.013961	0.000573	0.282456	0.000025	53	0.282456	−10.03	1.11
5	0.043137	0.001666	0.282457	0.000026	53	0.282455	−10.03	1.14
6	0.037480	0.001500	0.282470	0.000023	55	0.282468	−9.55	1.12
7	0.030792	0.001223	0.282475	0.000021	53	0.282474	−9.38	1.10
8	0.034314	0.001356	0.282479	0.000021	53	0.282478	−9.25	1.10
9	0.034297	0.001355	0.282480	0.000021	55	0.282478	−9.19	1.10
10	0.027901	0.001119	0.282483	0.000020	49	0.282482	−9.19	1.09
11	0.023001	0.000924	0.282485	0.000022	53	0.282484	−9.05	1.08
12	0.037949	0.001493	0.282489	0.000017	51	0.282488	−8.93	1.09
13	0.028050	0.001114	0.282490	0.000025	56	0.282489	−8.79	1.08
14	0.022061	0.000885	0.282496	0.000020	53	0.282496	−8.61	1.07
15	0.022043	0.000884	0.282497	0.000020	53	0.282497	−8.58	1.06
16	0.032171	0.001290	0.282498	0.000023	53	0.282496	−8.60	1.08
17	0.023309	0.000953	0.282505	0.000022	52	0.282504	−8.34	1.06
18	0.043951	0.001724	0.282519	0.000021	51	0.282517	−7.90	1.06
19	0.040206	0.001576	0.282583	0.000036	60	0.282581	−5.44	0.96
YJ-23								
1	0.029370	0.001026	0.282392	0.000015	56	0.282390	−12.35	1.22
2	0.065167	0.002425	0.282615	0.000018	52	0.282613	−4.50	0.94
3	0.024066	0.000962	0.282576	0.000016	50	0.282575	−5.84	0.96
4	0.029111	0.001135	0.282578	0.000018	50	0.282577	−5.76	0.96
5	0.038544	0.001440	0.282549	0.000018	53	0.282547	−6.81	1.01
6	0.033083	0.001240	0.282546	0.000018	51	0.282545	−6.89	1.01
7	0.026531	0.001025	0.282539	0.000016	52	0.282538	−7.14	1.01
8	0.030845	0.001195	0.282546	0.000017	51	0.282545	−6.88	1.00
9	0.032795	0.001240	0.282527	0.000022	50	0.282526	−7.56	1.03
10	0.031177	0.001176	0.282521	0.000018	51	0.282520	−7.78	1.04
11	0.009631	0.000354	0.282409	0.000018	52	0.282409	−11.72	1.17
12	0.024257	0.000927	0.282545	0.000019	53	0.282544	−6.92	1.00
13	0.026508	0.000925	0.282381	0.000018	53	0.282380	−12.72	1.23
14	0.024284	0.000961	0.282564	0.000017	54	0.282563	−6.26	0.97
15	0.035270	0.001372	0.282551	0.000018	49	0.282550	−6.71	1.00
16	0.024167	0.000926	0.282542	0.000019	50	0.282541	−7.03	1.00
17	0.020027	0.000794	0.282536	0.000018	52	0.282535	−7.24	1.01
18	0.023117	0.000896	0.282521	0.000026	56	0.282520	−7.77	1.03
19	0.030958	0.001196	0.282549	0.000018	53	0.282548	−6.78	1.00
20	0.032559	0.001286	0.282535	0.000019	53	0.282533	−7.30	1.02
21	0.040930	0.001579	0.282534	0.000019	54	0.282532	−7.35	1.03
22	0.019890	0.000782	0.282500	0.000018	48	0.282499	−8.51	1.06
23	0.036798	0.001421	0.282536	0.000020	52	0.282534	−7.27	1.02
LD-1								
1	0.023147	0.000912	0.282610	0.000014	56	0.282609	−4.53	0.91
2	0.025699	0.001012	0.282582	0.000011	53	0.282581	−5.60	0.95
3	0.030210	0.001192	0.282607	0.000014	54	0.282606	−4.70	0.92
4	0.030688	0.001240	0.282577	0.000013	60	0.282576	−5.63	0.96
5	0.024354	0.000958	0.282580	0.000013	58	0.282579	−5.56	0.95

Table 2 (*continued*)

Sample spot	$^{176}Yb/^{177}Hf$	$^{176}Lu/^{177}Hf$	$^{176}Hf/^{177}Hf$	2σ	$^{206}Pb/^{235}U$ age (Ma)	$^{176}Hf/^{177}Hf$ (t)	ε_{Hf} (t)	T_{dm} (Ga)
6	0.031178	0.001222	0.282598	0.000013	58	0.282597	−4.93	0.93
7	0.009962	0.000373	0.282485	0.000015	55	0.282485	−8.96	1.07
8	0.030115	0.001204	0.282573	0.000014	54	0.282572	−5.89	0.97
9	0.033559	0.001340	0.282604	0.000011	57	0.282602	−4.75	0.93
10	0.024958	0.000977	0.282562	0.000012	58	0.282561	−6.20	0.98
11	0.023640	0.000925	0.282609	0.000015	60	0.282608	−4.50	0.91
12	0.030476	0.001175	0.282586	0.000011	54	0.282585	−5.44	0.95
13	0.024867	0.000970	0.282588	0.000014	65	0.282587	−5.13	0.94
14	0.024163	0.000927	0.282610	0.000012	57	0.282609	−4.51	0.91
15	0.028879	0.001124	0.282574	0.000012	57	0.282573	−5.79	0.96
16	0.031791	0.001209	0.282604	0.000012	57	0.282603	−4.73	0.92
17	0.014467	0.000569	0.282589	0.000013	55	0.282588	−5.29	0.93
18	0.028424	0.001092	0.282644	0.000014	51	0.282643	−3.43	0.86
19	0.042616	0.001525	0.282562	0.000013	55	0.282560	−6.28	0.99
20	0.035915	0.001353	0.282606	0.000015	55	0.282604	−4.72	0.92
21	0.029250	0.001135	0.282596	0.000012	58	0.282595	−5.00	0.93
22	0.030315	0.001177	0.282571	0.000011	57	0.282570	−5.89	0.97
23	0.030872	0.001205	0.282593	0.000012	57	0.282591	−5.14	0.94
24	0.069652	0.002594	0.282577	0.000014	56	0.282575	−5.76	1.00
CBZ-4								
1	0.025820	0.001012	0.282775	0.000012	69	0.282774	1.59	0.68
2	0.039264	0.001565	0.282731	0.000014	68	0.282729	−0.02	0.75
3	0.027158	0.001094	0.282825	0.000014	68	0.282823	3.31	0.61
4	0.031079	0.001253	0.282805	0.000012	67	0.282804	2.59	0.64
5	0.030752	0.001259	0.282815	0.000013	65	0.282814	2.91	0.62
6	0.019616	0.000815	0.282847	0.000015	68	0.282846	4.09	0.57
7	0.032083	0.001276	0.282790	0.000012	65	0.282789	2.02	0.66
8	0.036680	0.001412	0.282790	0.000011	63	0.282788	1.96	0.66
9	0.030566	0.001219	0.282803	0.000014	69	0.282802	2.56	0.64
10	0.037867	0.001536	0.282832	0.000014	69	0.282830	3.56	0.60
11	0.023156	0.000934	0.282768	0.000014	68	0.282766	1.29	0.69
12	0.040929	0.001614	0.282795	0.000012	69	0.282793	2.24	0.66
13	0.028723	0.001155	0.282780	0.000013	63	0.282779	1.62	0.67
14	0.027419	0.001108	0.282780	0.000013	66	0.282779	1.70	0.67
15	0.023152	0.000946	0.282785	0.000013	65	0.282783	1.83	0.66
16	0.030260	0.001176	0.282800	0.000012	73	0.282799	2.55	0.64
17	0.035024	0.001399	0.282817	0.000013	63	0.282815	2.91	0.62
18	0.033257	0.001342	0.282811	0.000014	66	0.282810	2.78	0.63
19	0.059272	0.002189	0.282803	0.000011	64	0.282800	2.41	0.66
20	0.032193	0.001283	0.282819	0.000014	60	0.282818	2.94	0.62
21	0.038262	0.001526	0.282799	0.000014	68	0.282797	2.39	0.65
22	0.016974	0.000709	0.282776	0.000011	56	0.282775	1.33	0.67
23	0.024994	0.001054	0.282772	0.000012	63	0.282771	1.34	0.68
24	0.026105	0.001042	0.282799	0.000012	67	0.282798	2.39	0.64
25	0.019152	0.000787	0.282795	0.000012	69	0.282794	2.30	0.64
CBZ-6								
1	0.070649	0.002753	0.282644	0.000013	68	0.282640	−3.18	0.90
2	0.035272	0.001376	0.282639	0.000014	68	0.282638	−3.26	0.88
3	0.061401	0.002577	0.282699	0.000013	64	0.282696	−1.29	0.82
4	0.059624	0.002373	0.282670	0.000013	72	0.282667	−2.16	0.86
5	0.022674	0.000900	0.282673	0.000014	85	0.282671	−1.70	0.82
6	0.040269	0.001616	0.282759	0.000014	69	0.282757	0.97	0.71
7	0.041212	0.001644	0.282652	0.000013	70	0.282650	−2.79	0.86
8	0.036442	0.001442	0.282796	0.000016	89	0.282794	2.73	0.65
9	0.079154	0.003069	0.282692	0.000015	79	0.282687	−1.27	0.84
10	0.040866	0.001609	0.282865	0.000014	67	0.282863	4.69	0.56
11	0.113774	0.004284	0.282789	0.000014	66	0.282784	1.88	0.72
12	0.049244	0.001951	0.282636	0.000013	70	0.282633	−3.38	0.90
13	0.034758	0.001365	0.282560	0.000012	74	0.282558	−5.93	0.99
14	0.057672	0.002251	0.282812	0.000014	75	0.282809	2.96	0.64
15	0.078243	0.003027	0.282711	0.000013	68	0.282707	−0.79	0.81
16	0.055182	0.002248	0.282717	0.000012	70	0.282714	−0.50	0.78
17	0.100924	0.003877	0.282752	0.000014	71	0.282746	0.65	0.77
18	0.038099	0.001505	0.282702	0.000011	74	0.282700	−0.93	0.79
19	0.058246	0.002310	0.282769	0.000012	72	0.282766	1.35	0.71
20	0.054025	0.002132	0.282698	0.000012	71	0.282695	−1.16	0.81
NB-18								
1	0.031751	0.001280	0.282785	0.000013	53	0.282784	1.58	0.67
2	0.026036	0.001052	0.282808	0.000011	54	0.282807	2.43	0.63
3	0.026002	0.001035	0.282806	0.000011	56	0.282805	2.39	0.63
4	0.035205	0.001313	0.282756	0.000012	53	0.282755	0.55	0.71
5	0.028042	0.001139	0.282814	0.000012	53	0.282813	2.60	0.62
6	0.047851	0.001896	0.282752	0.000012	53	0.282750	0.38	0.73
7	0.026818	0.001078	0.282803	0.000012	54	0.282802	2.24	0.64

(*continued on next page*)

Table 2 (*continued*)

Sample spot	$^{176}Yb/^{177}Hf$	$^{176}Lu/^{177}Hf$	$^{176}Hf/^{177}Hf$	2σ	$^{206}Pb/^{235}U$ age (Ma)	$^{176}Hf/^{177}Hf$ (t)	ε_{Hf} (t)	T_{dm} (Ga)
8	0.023580	0.000963	0.282814	0.000013	55	0.282813	2.65	0.62
9	0.030581	0.001188	0.282834	0.000013	56	0.282833	3.39	0.60
10	0.047860	0.001805	0.282727	0.000012	55	0.282725	−0.44	0.76
11	0.030139	0.001258	0.282821	0.000012	54	0.282820	2.89	0.61
12	0.024060	0.000998	0.282821	0.000012	53	0.282820	2.86	0.61
13	0.023778	0.000973	0.282761	0.000014	53	0.282760	0.75	0.69
14	0.025001	0.001027	0.282791	0.000012	54	0.282790	1.80	0.65
15	0.031527	0.001225	0.282831	0.000017	55	0.282830	3.26	0.60
16	0.019501	0.000753	0.282750	0.000011	52	0.282749	0.33	0.71
17	0.066751	0.002722	0.282763	0.000010	57	0.282760	0.81	0.73
18	0.037579	0.001457	0.282788	0.000014	56	0.282786	1.74	0.67
19	0.018848	0.000759	0.282776	0.000012	55	0.282776	1.33	0.67
20	0.022689	0.000929	0.282803	0.000011	56	0.282802	2.28	0.64
21	0.033305	0.001296	0.282731	0.000014	53	0.282730	−0.32	0.74
22	0.030063	0.001172	0.282727	0.000012	53	0.282726	−0.47	0.75
23	0.026323	0.001092	0.282775	0.000011	52	0.282774	1.22	0.68
24	0.025381	0.001045	0.282782	0.000013	51	0.282781	1.43	0.67
25	0.031739	0.001266	0.282754	0.000013	52	0.282752	0.44	0.71

$(^{176}Lu/^{177}Hf)_{CHUR} = 0.0332$; $(^{176}Hf/^{177}Hf)_{CHUR,O} = 0.282772$ (Blichert-Toft and Albarede, 1997); $(^{176}Lu/^{177}Hf)_{DM} = 0.0384$; $(^{176}Hf/^{177}Hf)_{DM,O} = 0.28325$ (Griffin et al., 2006); $\lambda = 1.867 \times 10^{-11}$/year (Soderlund et al., 2004).

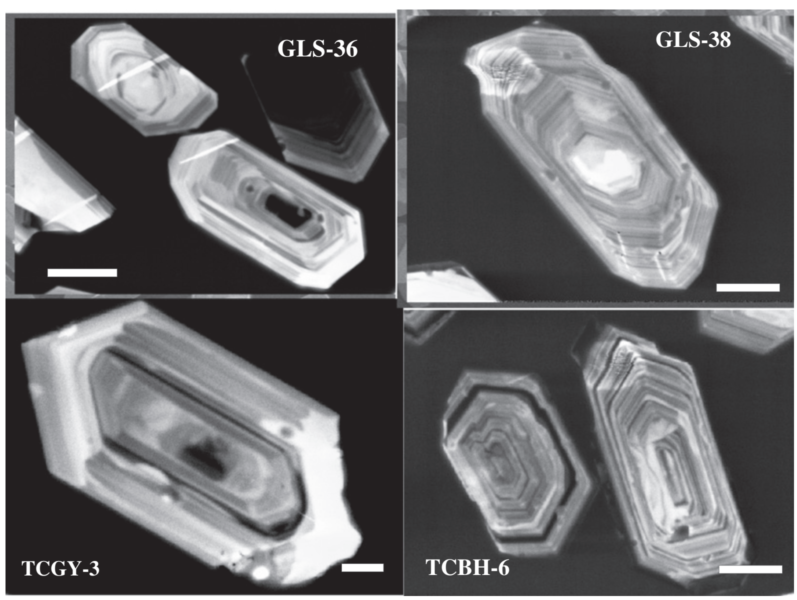

Fig. 3. Cathodoluminescence images of representative zircons extracted from the granitoids from the Gaoligong–Tengliang area. Scale bar = 100 μm.

south Thailand. In Burma, this old boundary is largely masked by the Tertiary sedimentary and volcanic rocks (Morley, 2004).

The eastern Highland is cut through by the Mogok metamorphic belt, which extends for over 1500 km along the western margin of the Shan-Thai block, from the Andaman Sea north to the eastern Himalaya syntaxis. It is composed of a variety of parageneisses, orthogneisses and migmatites. Recent structural analysis and geochronological data suggest that the MMB lines north to the unexposed middle or lower crust rocks of the Lhasa terrane (Searle et al., 2007). The exhumation of the MMB may be related to the oblique movement along the normal fault (Mitchell, 1993).

To sum up, the geology of Burma seems to have been influenced by the long term subduction of Indian oceanic plate and collisions between microcontinents. However, the relative importance between these processes remains ambiguous. In particular, the northward continuation of the S-type granites and the MMB is unclear in the region near the China–Burma border.

3. Field observation and petrographic characteristics

For convenience, the granites from Gaoligong, Tengliang and Yingjiang regions are described separately. The Gaoligong granites are medium grained K-feldspar-rich monzogranite, granodiorite and locally leucogranite. They show a rather simple mineral assemblage comprising K-feldspar (40%) + plagioclase (30%) + quartz (20–30%) + biotite (2–3%) ± muscovite ± apatite ± hornblende. The main ferromagnesian phases are biotite. Accessory phases include apatite, zircon and ilmenite. Cordierite, indicative of high temperature granite (Sylvester, 1998), is not found in the Gaoligong granites. The core of the Gaoligong granites is massive and coarse-grained. Those along the Nujiang fault display a strong deformation and foliation defined by subparallel plagiocase laths and large biotite laths (a few mm length). The S-type of the Gaoligong granites is also indicated by the absence of amphibole. Consistent with petrographic features, bulk rock analyses reveal a

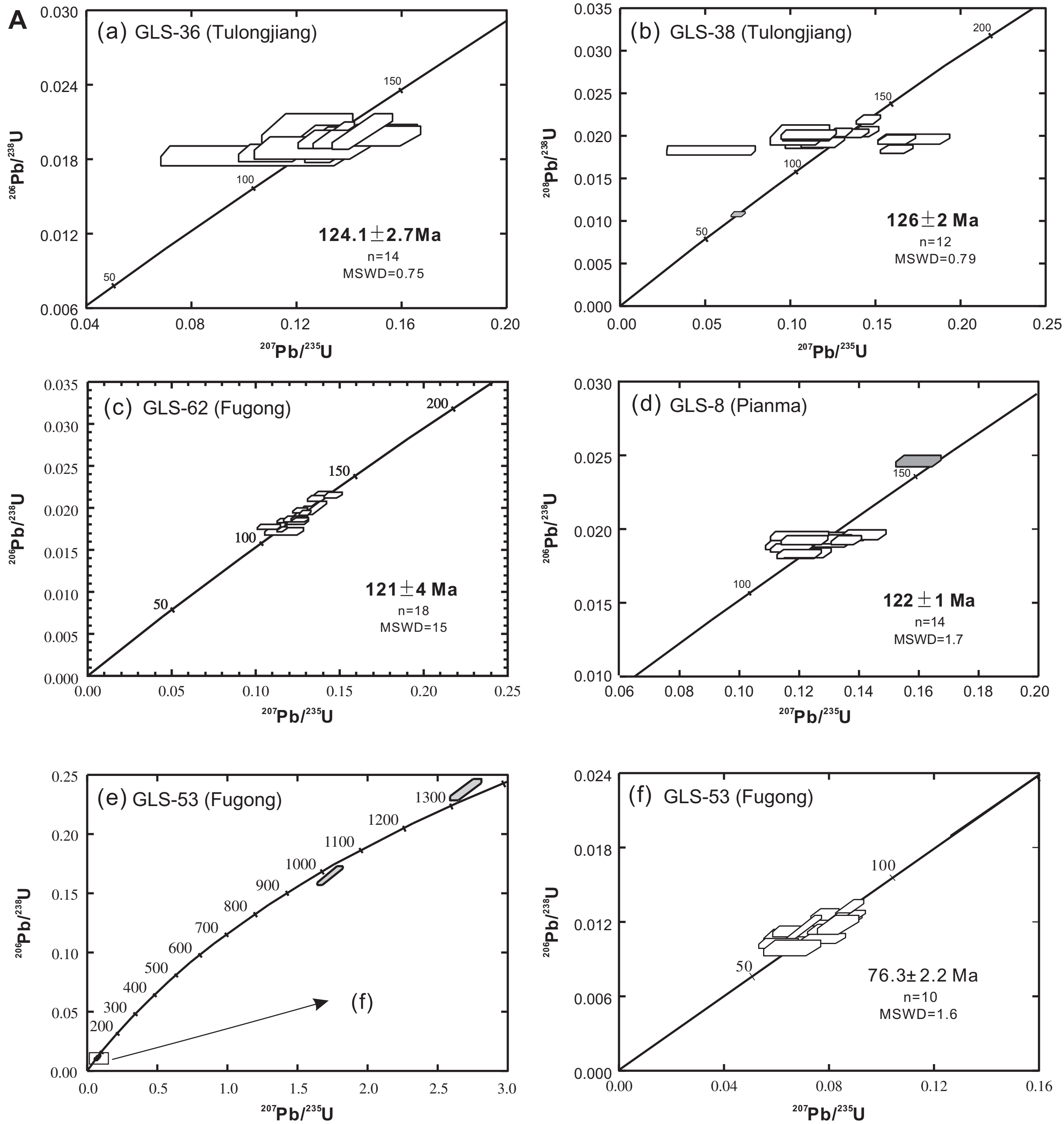

Fig. 4. SHRIMP zircon U–Pb concordia diagrams for the granitoids from the GTY area. (A) Gaoligong; (B) Tengliang and (C) Yingjiang.

peraluminous to strongly peraluminous character for the Gaoligong granites (Fig. 2b).

The Tengliang granites show a similar mineral assemblage as the Gaoligong batholith, with K-feldspar (35%) + plagioclase (35%) + quartz (20–30%) + biotite (3%) ± hornblende ± apatite. Differences between the Tengliang and Gaoligong granites are the absence of muscovite in the Tengliang suite.

The intrusions in the Yingjiang area exhibit a spatial variation in lithology. The granites in eastern Yingjiang show a petrographic feature similar to those in the Gaoligong and Tengliang area, with a strong peraluminous affinity. A typical example is the Lailishan granite with which tin-mineralization is associated. In contrast, the samples collected from western Yingjiang, i.e., the area between Tongbiguan, Nabang and Sudian (proximal to the China–Burma border), are characterized by the ubiquitous presence of hornblende, indicative of I-type granites. In ANK vs. A/CNK plot (Fig. 2b), the samples from west Yingjiang straddle the boundary between metaluminous and peraluminous fields. A number of gabbroic intrusions crop out in the western Yingjiang area (Fig. 1b).

4. Analytical techniques

Zircons were separated from fifteen samples using conventional heavy liquid and magnetic techniques and purified by hand-picking

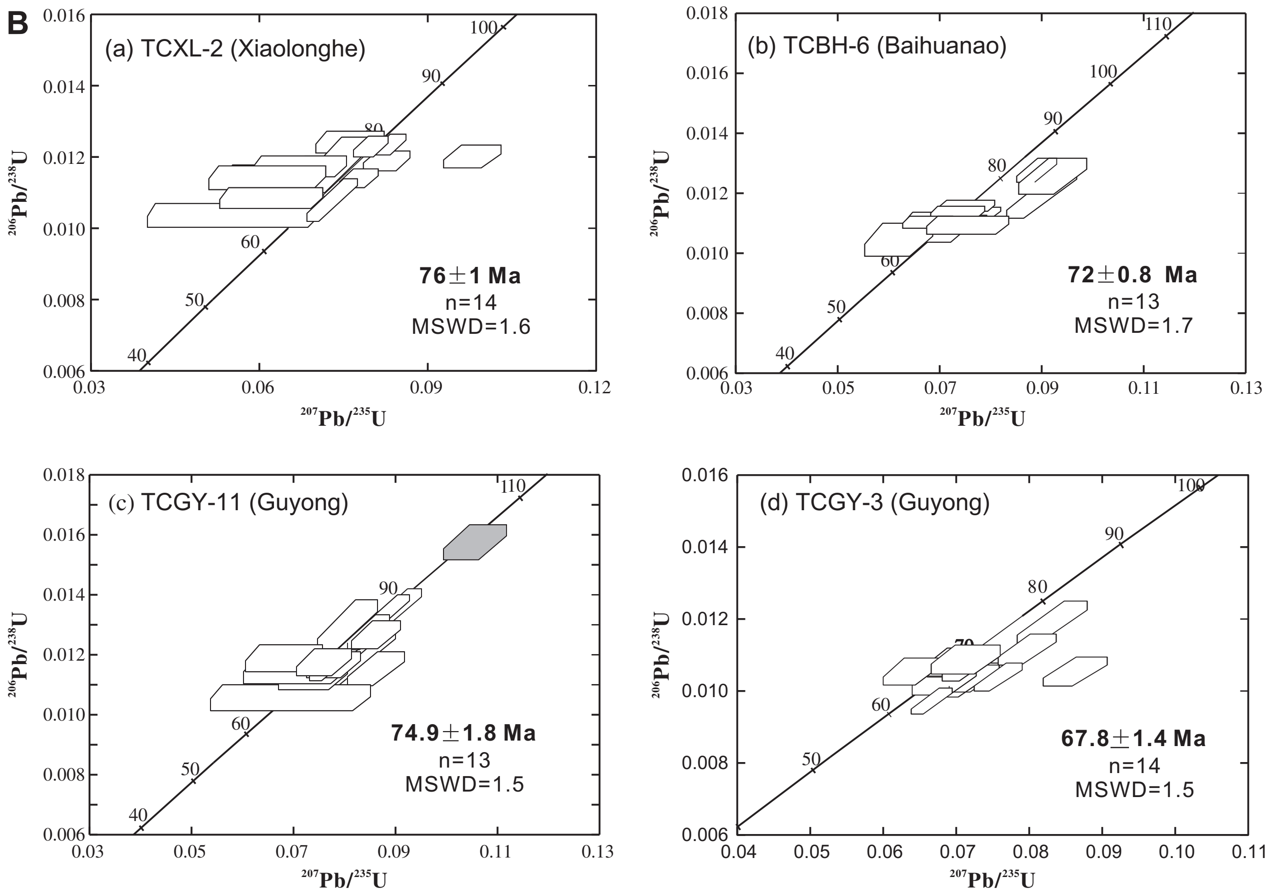

Fig. 4 (*continued*)

under a binocular microscope. Internal structure of zircons was examined using cathodoluminescence (CL) image techniques prior to U–Pb isotopic analyses. The U–Pb analyses of ten samples were performed using a Sensitive High-Resolution Ion Microprobe (SHRIMP II) at the Institute of Geology, Chinese Academy of Geological Sciences, Beijing. Detailed analytical procedures are similar to those described by Williams (1998). The standard TEM zircons (417 Ma) were used in interelement fractionation, and U, Th and Pb concentrations were determined based on the standard Sri Lankan gem zircon SL13 (572 Ma). Data processing was carried out using the SQUID 1.03 and Isoplot/Ex 2.49 programs of Ludwig (2001a,b), and the ^{204}Pb-based method of common Pb correction was applied. Other five samples were analyzed by Laser Ablation-Inductively Coupled Plasma Mass Spectrometry (LA-ICPMS, Agilent 7500a) at the State Key Laboratory of Geological Processes and Mineral Resources, China University of Geosciences. The laser-ablation system is a GeoLas 2005 (MicroLas, Gottingen, Germany), which is equipped with a 193 nm ArF-excimer laser and a homogenizing, imaging optical system. The conditions of 30 μm Spot Size and 80 Hz Energy Density were adopted. The standard 91,500 zircons were used for correction of interelement fractionation, and U, Th and Pb concentrations were determined based on the standard NIST610. The Glitter program (version 4.0) was used for raw data reduction and age calculation, and the ^{204}Pb-based method of common Pb correction was applied for the samples. Detailed procedures are similar to those described by Yuan et al. (2004). Uncertainties of data points reported in Table 1 and Table 2 are given at $\pm 1\sigma$. All the ages quoted in the text are ^{207}Pb/^{206}Pb ages or ^{206}Pb/^{238}U ages, which are the weighted mean at the 95% confidence level.

In-situ zircon Hf isotopic analyses were carried out on the dated spots using the Neptune MC-ICPMS, equipped with a 193 nm laser, at the Institute of Geology and Geophysics, Chinese Academy of Sciences in Beijing, China. During analyses, spot sizes of 31 or 63 μm, with a laser repetition rate of 6 Hz at 100 mJ, were used. The detailed analytical technique and data correction procedure are described in Wu et al. (2006). During analyses, the ^{176}Hf/^{177}Hf and ^{176}Lu/^{177}Hf ratios of the standard zircon (91,500) were 0.282294 ± 15 ($2\sigma_n$, $n = 20$) and 0.00031, similar to the low peaks of ^{176}Hf/^{177}Hf ratios of 0.282284 ± 22 measured using the laser method (Griffin et al., 2006).

5. Results

5.1. U–Pb zircon chronology

The results of U–Pb zircon analyses for sixteen granites from the studied area are listed in Table 1. Zircons display well-developed tetragonal dipyramids and magmatic zoning (Fig. 3). These zircon grains have a relatively wide range in U (323–4538 ppm) and Th (261–2172 ppm) concentrations. Th/U ratios of these zircons are greater than 0.4. This, together with oscillatory zoning, is suggestive of a magmatic origin (Hoskin and Schaltegger, 2003). Thus, the interpretation of the U–Pb data is rather simple and the obtained ages are interpreted as the timing of emplacement of the granites.

5.1.1. Gaoligong granites

Sample GLS-36 and GLS-38 were collected in the northern part of the GTY belt, during a traverse from Gongshan to Dulongjiang

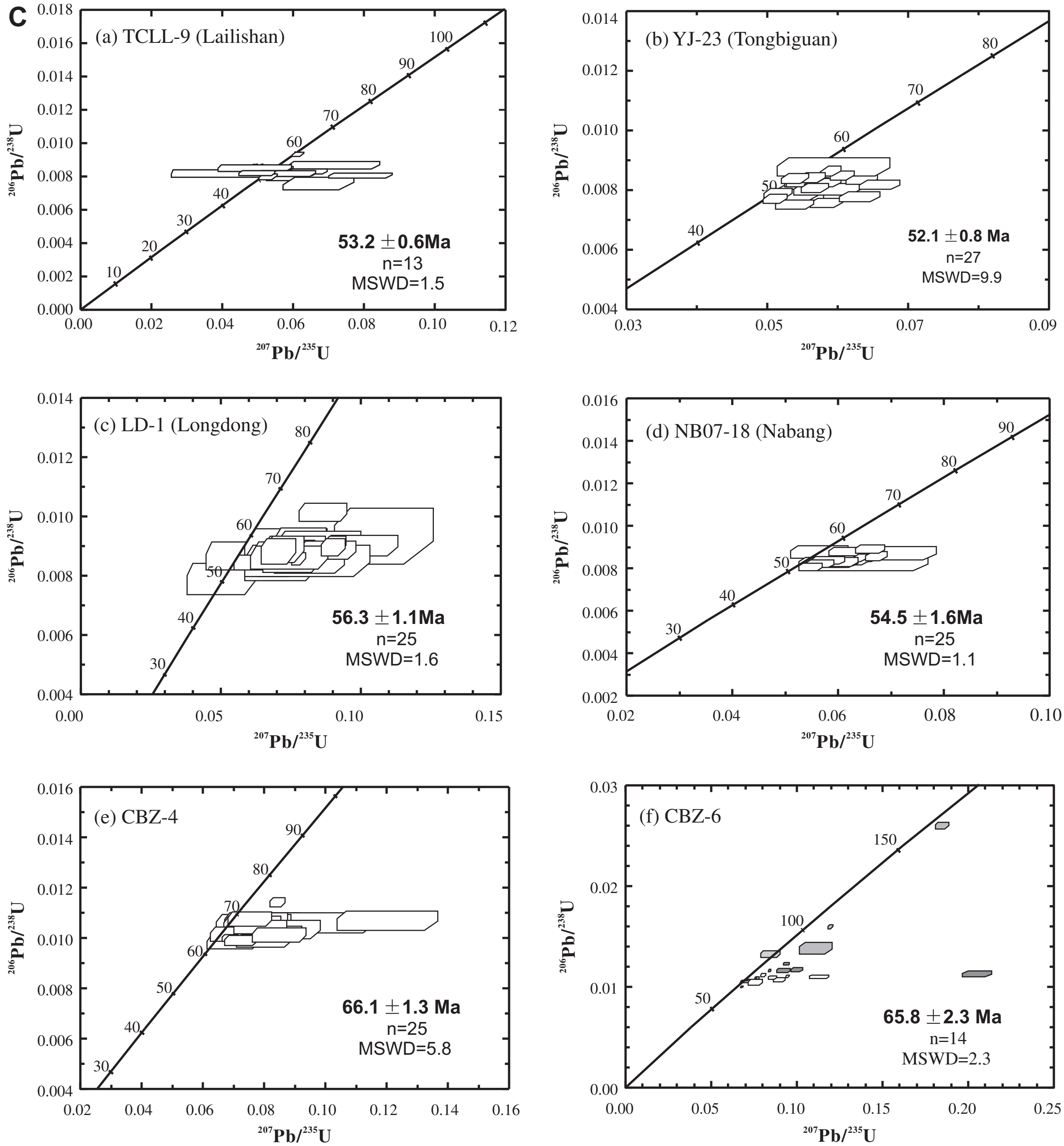

Fig. 4 (*continued*)

(Fig. 1b). Both samples are a coarse-grained monzogranite mainly consisting of plagioclase, K-feldspar and quartz. Fourteen analyses on 14 zircons from sample GLS-36 form a tight cluster on the concordia plot (Fig. 4A-a) with a weighted mean $^{206}Pb/^{238}U$ age of 124.1 ± 2.7 Ma. This is interpreted to represent the crystallization age of the magmatic zircons. Twelve analyses of 12 zircons from sample GLS-38 yield a weighted mean $^{206}Pb/^{238}U$ age of 126 ± 2 Ma (Fig. 4A-b), which is identical within the error from that obtained for GLS-36. One grain that is morphologically indistinguishable from the main zircon population yields a younger age (68 ± 1.7 Ma).

Sample GLS-62, collected near Fugong in the middle part of the Gaoligong belt (Fig. 1b), shows a slightly younger age. Eighteen analyses yield a concordant $^{206}Pb/^{238}U$ age of 121 ± 4 Ma (Fig. 4A-c). Fourteen analyses of 14 zircons from GLS-8, which is collected near Lushui in the southern part of the Gaoligong belt, are concordant, yielding a weighted mean $^{206}Pb/^{238}U$ age of 122 ± 2 Ma (Fig. 4A-d). One grain that is morphologically indistinguishable from the main zircon population yields an older age (153 ± 3 Ma).

Unlike the Early Cretaceous emplacement ages (121–126 Ma) found for four samples collected from spatially distant regions of the Gaoligong belt, a distinctly younger age is obtained for the sample GLS-53, which is a leucocratic granite that intrudes the main Early Cretaceous granitic body near Fugong. Ten analyses are concordant, with a weighted mean $^{206}Pb/^{238}U$ age of 76.3 ± 2 Ma (Fig. 4A-f). This is interpreted as the age of magmatic overgrowth corresponding to the time of emplacement. The remaining analyses give Precambrian ages with $^{207}Pb/^{206}Pb$ dates ranging from 984 Ma to 1373 Ma (Table 1, Fig. 4A-e). This is taken

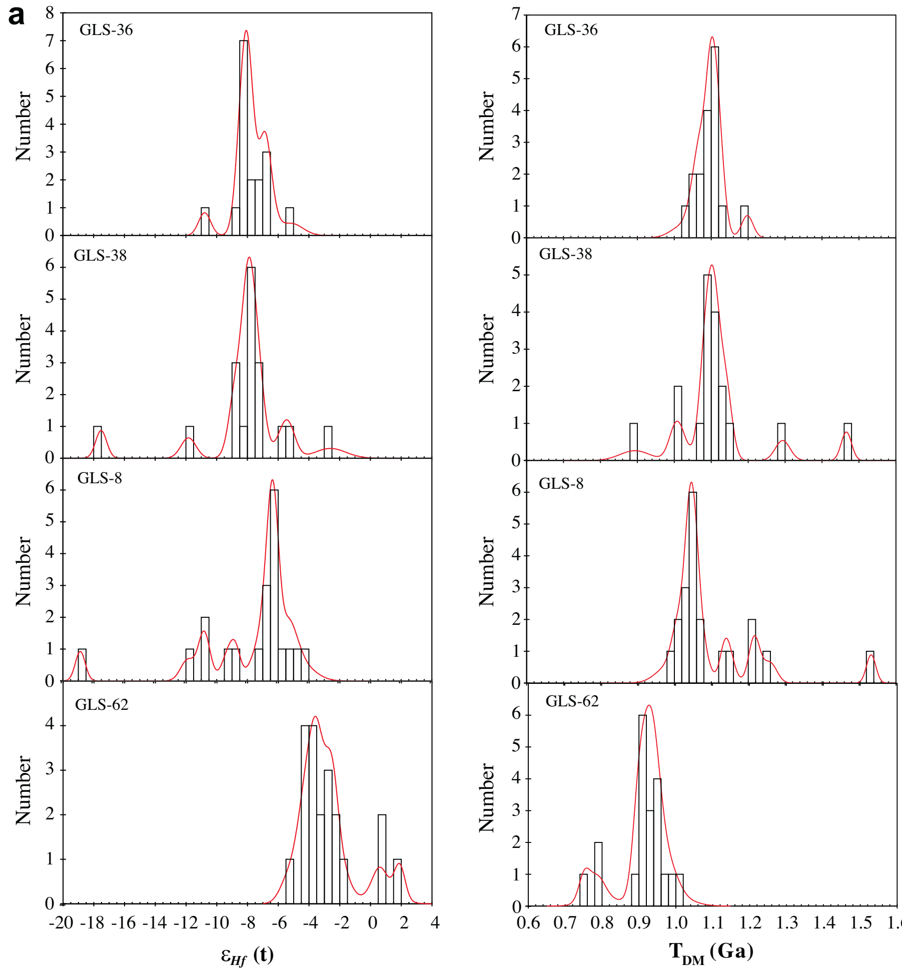

Fig. 5. Histograms of initial Hf isotope ratio (left hand) and Hf model ages (right hand) for zircons of (a) Early Cretaceous, (b) Late Cretaceous and (c) Early Cenozoic ages.

to represent the protolith age of the source materials. The scatter and disconcordance of the ages for the inherited zircons may be partly due to an episode of ancient lead loss and original differences in age of the protolith.

5.1.2. Tengliang granites

Four granite samples from the Tengliang area were selected for U–Pb dating. TCXL-2 is a leucocratic granite collected at Xiaolonghe (Fig. 1b). Analyses of 14 zircons (Table 1) yield concordant ages, with a weighted mean $^{206}Pb/^{238}U$ age of 76 ± 1 Ma (Fig. 4B-a). This age is considerably younger than the main time span of granitic magmatism in the Gaoligong area, but is identical within errors to that for leucocratic intrusion in Early Cretaceous body near Fugong.

A similar age (72 ± 0.8 Ma) is obtained for a granitic sample collected at Baihuanao (Fig. 4B–b). Two samples from Guyong (TCGY-3 and TCGY-11) are coarse-grained monzonites. Fourteen and thirteen analyses on zircons of these two samples yield concordant $^{206}Pb/^{238}U$ age of 67.8 ± 1.4 Ma and 74.9 ± 1.8 Ma, respectively (Fig. 4c and d). One grain in TCGY-11 yields an age at 100 ± 3 Ma, which is significantly older than that for the main zircon population.

5.1.3. Yingjiang granites

The youngest ages are found for the plutons in Yingjiang area, southwestmost of the study area (Fig. 1b). Thirteen analyses on zircons of the Lailishan sample (TCLL-9, eastern Yingjiang) yield a concordant $^{206}Pb/^{238}U$ age of 53.2 ± 0.6 Ma (Fig. 4C-a). A similar age (52.1 ± 0.8 Ma) is obtained for the Tongbiguan sample (YJ-23; Fig. 4C-b), collected in the middle way to the China–Burma border (Fig. 1b), while a slightly older age (56.3 ± 1.1 Ma) is obtained for the sample (LD-1) from Longdong, north of Kazhang township (Fig. 4C-c).

Three samples have been collected in western Yingjiang, near the China–Burma border. One I-type granite from Nabang yield a concordant $^{206}Pb/^{238}U$ age of 54.5 ± 1.6 Ma (Fig. 4C-d). Relatively older ages (ca. 66 Ma) are obtained for the two samples collected at Caobazhai, west Kachang (Fig. 4C-e and -f). Twenty-five analyses on zircons of CBZ-4 yield a concordant $^{206}Pb/^{238}U$ age of 66.1 ± 1.3 Ma (Fig. 4C-e). The analyses for CBZ-6 show a complex picture. One grain yields a $^{206}Pb/^{238}U$ age of 984 Ma (Table 1), indicating its inherited nature. The remaining twenty-two analyses yield disconcordant ages ranging between 64 and 165 Ma. Interpretation of these ages remains problematic. It is noted that fourteen analyses yield ages between 64 and 72 Ma, and proximal to the concordant curve. The average age (65.8 ± 2.3 Ma) of these analyses is thus tentatively interpreted as the emplacement age.

5.1.4. Temporal and spatial distribution of batholiths in the GTY area

The U–Pb isotope analyses on zircons extracted from granites in the GTY belt reveal three main pulses of magmatism in the east of the eastern Himalaya Syntaxis, namely early Cretaceous, late Cretaceous and Early Cenozoic (Fig. 4). Moreover, magmatism seems to migrate with time from NE to SE. Specifically, the Gaoligong

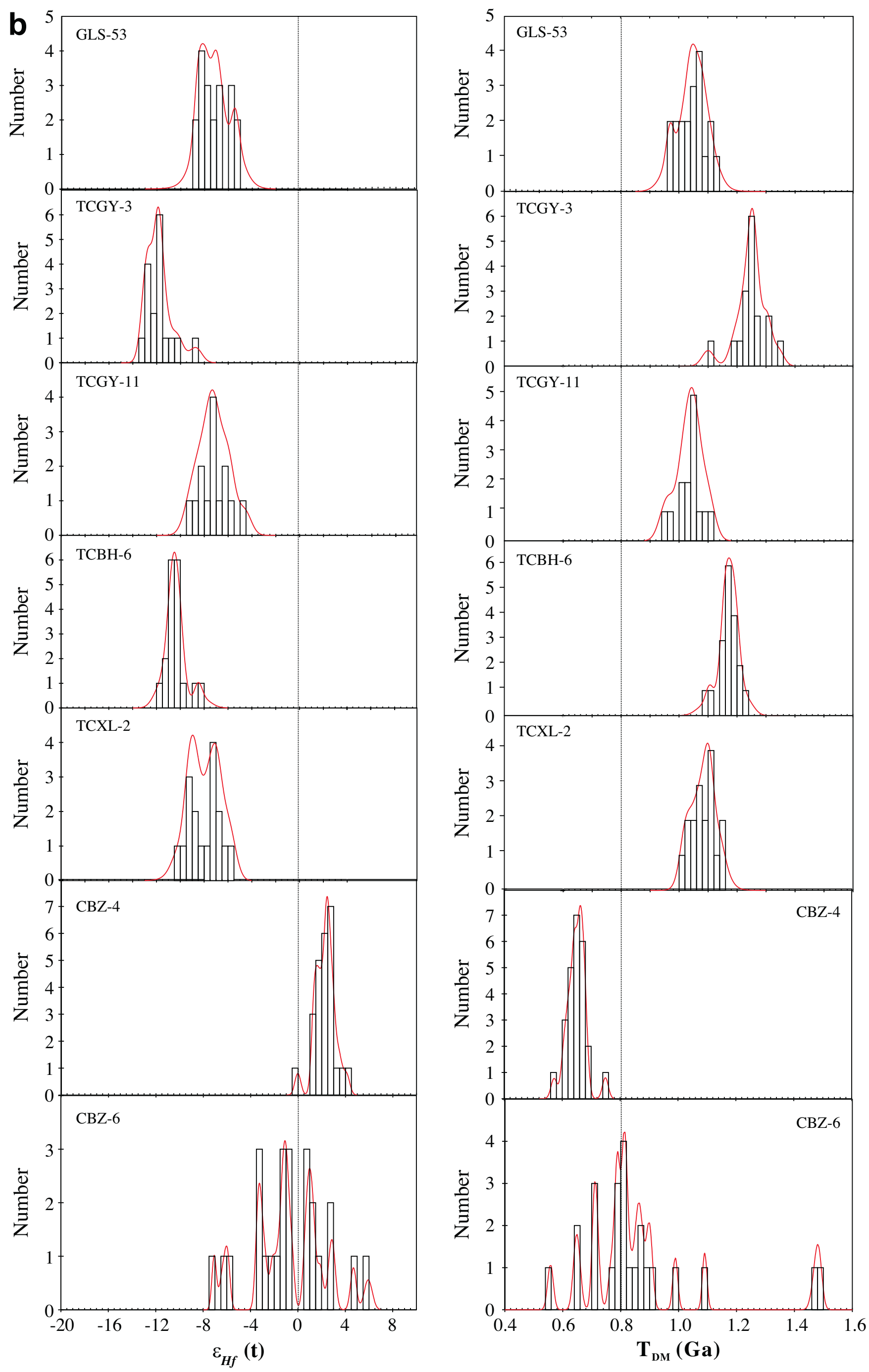

Fig. 5 (*continued*)

granites in the northeast were mainly emplaced during the Early Cretaceous, whereas the Tengliang granites in southwest of the studied area (north of Tengchong county) were emplaced during the late Cretaceous (Fig. 1b). The youngest episode (52–66 Ma) is found for the Yingjiang granites which are located to southwest-most of the study region, proximal to the China–Burma border (Fig. 1b). Collectively, currently available geochronologic data reveal a southwestward younging of magmatism in the GTY area.

5.2. Zircon Hf isotopes and model ages

In-situ zircon Hf isotope data of two hundred zircon grains from sixteen granitoids of the Gaoligong–Tengliang batholiths are listed in Table 2. The initial Hf isotope ratios are calculated at emplacement age, using the ^{176}Lu–^{176}Hf decay constant reported in Soderlund et al. (2004). ^{176}Lu/^{177}Hf ratios of most zircons are less than 0.003, indicating a low radiogenetic growth of ^{176}Hf. The single stage depleted-mantle model ages (T_{DM}) are determined for each sample (Table 2) by calculating the intersection of the zircon/parent-rock growth trajectory with the depleted-mantle evolution curve (Vervoort and Blichert-Toft, 1999).

Zircons from three early Cretaceous Gaoligong granites (GLS-36, 38, 8) show essentially similar Hf isotope compositions, with most having $\varepsilon_{Hf}(t)$ ranging between −10 to −4 (Fig. 5a). The averaged $\varepsilon_{Hf}(t)$ of GLS-36, GLS-38 and GLS-8 are between −6 and −8, corresponding to single model ages of 1042–1108 Ma (Fig. 5a).

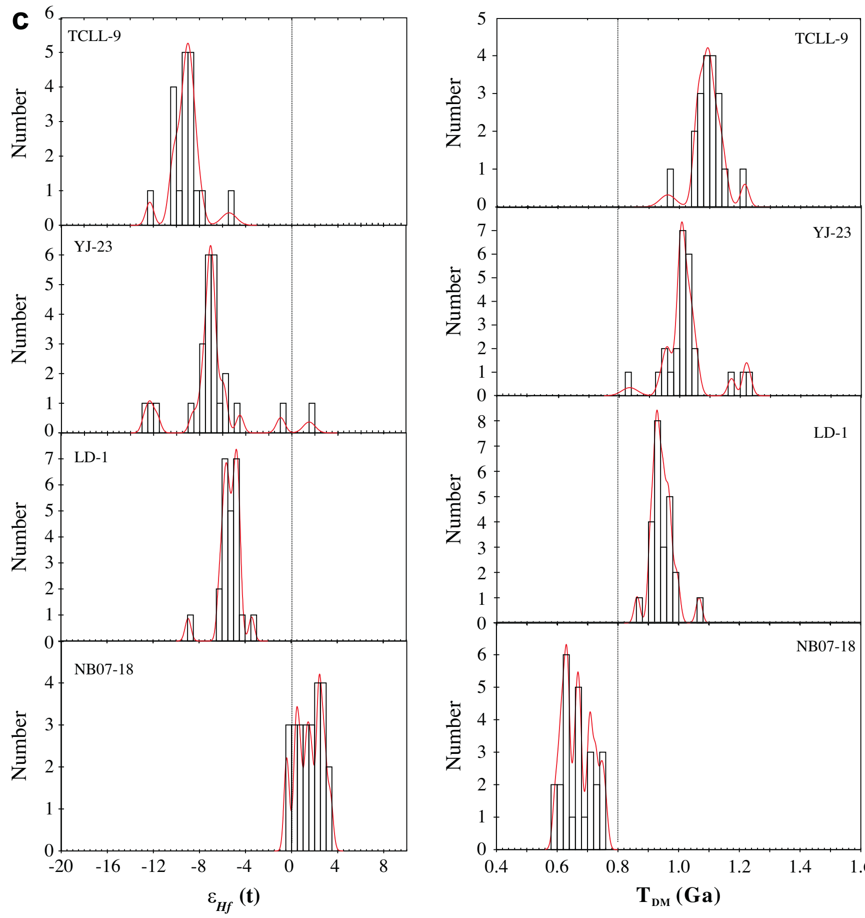

Fig. 5 (*continued*)

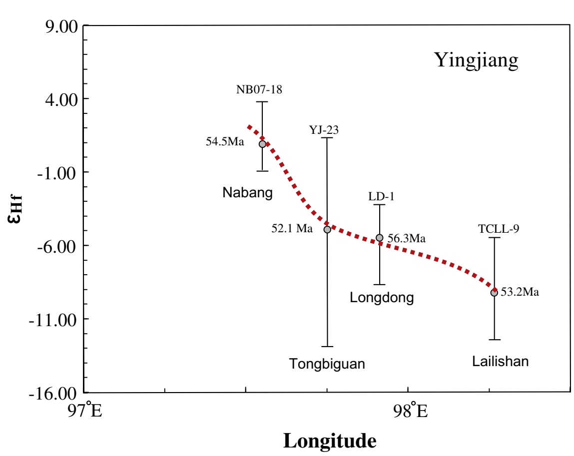

Fig. 6. East–west variation of average ε_{Hf} in zircons from Early Cretaceous granites from Yingjiang.

Relatively higher $\varepsilon_{Hf}(t)$ values (1.9 to −5.4) are observed for the sample GLS-62, which displays a weakly bimodal distribution in both initial Hf isotope ratio and Hf model age (Fig. 5). Seventeen analyses have $\varepsilon_{Hf}(t)$ values of −5.4 to −1.9 with a weighted mean of −3.4, corresponding to an averaged T_{DM} age of 930 Ma. The remaining three analyses give positive $\varepsilon_{Hf}(t)$ values of 0.6–1.9, corresponding to relatively young T_{DM} ages of 750–790 Ma.

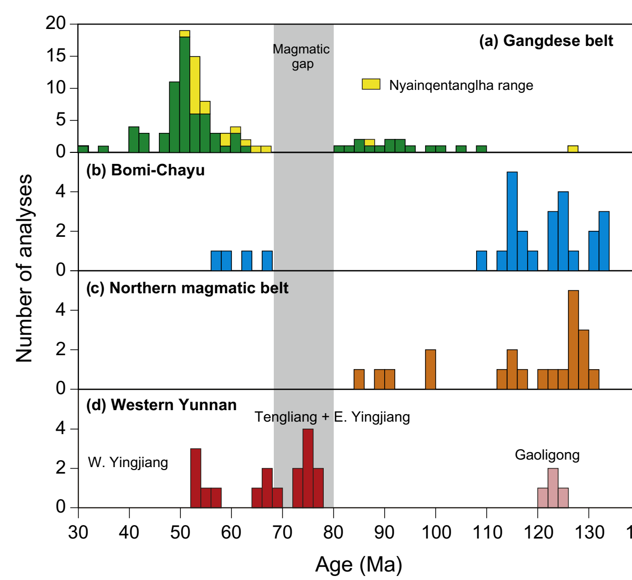

Fig. 7. Comparison of emplacement ages of the GTY batholiths with those of the Gangdese arc magmas, the northern magmatic belt and Bomi–Chayu. Note that the ages of the Gaoligong batholith are similar with that of the northern magmatic belt, whereas some of Tengliang granitoids were emplaced during a period that corresponds to the magmatic quiescence in the Lhasa Terrane. Data for the Gangdese batholiths and granitoids in the northern magmatic belt are after Wen et al. (2008) and Ji et al. (2009).

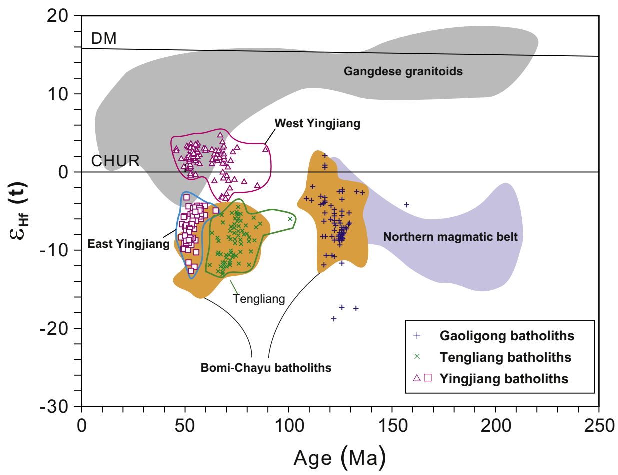

Fig. 8. Plot of zircon $\varepsilon_{Hf}(t)$ vs. U–Pb ages. For comparison, the fields of the Gangdese batholith (Chu et al., 2006) and Bomi–Chayu batholiths (Liang et al., 2008) are outlined.

With the exception of two samples (CBZ-4 & -6) collected in western Yingjiang area, the samples of the late Cretaceous magmatic episodes (mainly in the Tengliang area) show negative $\varepsilon_{Hf}(t)$ values, ranging between −4.6 and −13 (Fig. 5b), which are slightly lower than the values observed for the Gaoligong batholiths. The averaged values of individual plutons range between −7 and −12, with corresponding model ages of 1093 to 1260 Ma. Among the five plutons analyzed, sample TCGY-3 yields the lowest $\varepsilon_{Hf}(t)$ (−12) and the highest model age (1260 Ma). Two samples from Caobazhai (western Yingjiang area) exhibit positive $\varepsilon_{Hf}(t)$ values. While sample CBZ-4 shows a restricted range in $\varepsilon_{Hf}(t)$ (0–4) with corresponding model ages of 550–800 Ma, CBZ-6 exhibits a wide range in $\varepsilon_{Hf}(t)$ (−8∼+6).

Hf isotopic compositions of the youngest plutons from Yingjiang area delineate an east–west variation, with $\varepsilon_{Hf}(t)$ values increasing progressively from east Yingjiang to west Yingjiang (Fig. 5c and Fig. 6). The sample from east Yingjiang (TCLL-9) shows an Hf isotopic composition ($\varepsilon_{Hf}(t) = -12\sim-8$) indistinguishable from the older plutons (Fig. 6), indicative of old crustal provenance. In contrast, $\varepsilon_{Hf}(t)$ values for granites collected near the China–Burma border are positive (Fig. 5c and Fig. 6). Such a spatial variation in Hf isotopic composition is consistent with the lithologic variation with I-type granites occurring exclusively in west Yingjiang and S-type granites in east Yingjiang.

In summary, the overwhelmingly negative $\varepsilon_{Hf}(t)$ of the Gaoligong and Tengliang batholiths is in agreement with a derivation from a sedimentary source. The Hf model ages reported in this study are similar to the whole rock Nd model ages which vary between 1.0–1.4 Ga (Yang et al., 2006). A Mesoproterozoic metasedimentary source for the majority of the Gaoligong–Tengliang granites is also reflected in the presence of Proterozoic inherited zircons (Figs. 4A). Mantle contribution is evident in the samples near the China–Burma border and may be related to Neo-Tethyan subduction. Some intermediate compositions and model ages may reflect a mixing between a juvenile crust and an older (e.g., Mesoproterozoic) crust.

6. Comparison with magmatism in the Lhasa Terrane and in Burma

The GPS data illustrate eastward motion of the Tibetan Plateau which turns south along the Eastern Himalayan Syntaxis (Chen et al., 2000; Wang et al., 2001). The Gaoligong fault that bounds the Gaoligong granites to the east is a major intracontinental dextral strike-slip fault which possibly accommodates the extrusion of the Tibetan plateau (Wang et al., 2006). The western margin of the Gaoligong belt is Longchuanjiang, which runs parallel to the Indo-Burma suture in western Burma. The latter is considered as equivalent to the Yarlung–Tsangpo suture in Tibet. In this tectonic framework, the GTY area therefore occupies a similar tectonic position to the Lhasa terrane prior to and during the Indo-Asian collision. This is supported by the paleomagnetic studies (Li et al., 2004) and geologic reconstruction (Metcalfe, 1998), suggesting that the GTY area may represent the rotated, eastward extension of the Lhasa terrane. If this is the case, pre- and syn-collisional magmatism in these two regions should be comparable. On the other hand, it has been argued that the Shan-Thai Block is equivalent to the Lhasa Terrane (Mitchell, 1993; Searle et al., 2007) and the MMB extends from SE Asia to the eastern Himalayan Syntaxis. However the northward extension of this belt is unclear in the area near the Burma-China border. These issues will be addressed here by comparing the temporal and spatial distribution of granitic magmas in the GTY area with those in the Lhasa Block and in Burma.

6.1. Igneous activity in the Lhasa Terrane

Two magmatic belts have been identified in the Lhasa terrane, namely the Gangdese arc belt in south and the northern magmatic belt in north (Coulon et al., 1985; Chung et al., 2005; Chu et al., 2006). The Gangdese belt is composed of Jurassic, late Cretaceous

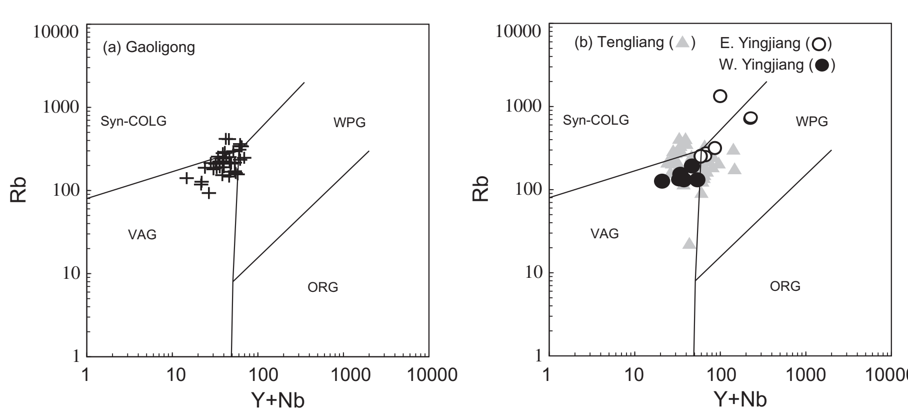

Fig. 9. Rb vs. (Y + Nb) discrimination diagram for (a) Gaoligong granites and (b) Tengliang and Yingjiang granites (after Pearce et al. (1984)). ORG = Ocean Ridge granites; Syn-COLG = syn-collisional granites; VAG = volcanic-arc granites; WPG = within-plate granites.

to Paleogene batholiths with I-type geochemical affinities, including gabbro, diorite, granodiorite, monzogranites and minor syenogranite (Debon et al., 1985; Chu et al., 2006; Wen et al., 2008; Ji et al., 2009), which are separated by a magmatic gap from 80 Ma to ~70 Ma (Wen et al., 2008; Ji et al., 2009; Fig. 7a). Arc magmatism resumed since ~70 Ma when the roll-back of flatly subducting Neo-Tethyan slab opened a window allowing the rising of asthenosphere (Wen et al., 2008). Subsequent break-off of oceanic plate resulted in magmatic flare-up at ~50 Ma (Ji et al., 2009). It is shown that over 87% of zircons from the Gangdese batholith have $\varepsilon_{Hf}(t)$ values greater than +5 (Chu et al., 2006; Ji et al., 2009; Fig. 8). This is corroborated with the positive whole rock $\varepsilon_{Nd}(t)$, suggesting their provenance from a juvenile mantle source. Wen et al. (2008) suggested that the Gangdese batholith resulted from remelting of the underplated lower crust above subducting Neo-Tethyan plate. All these indicate a long-lasting role of the Neo-Tethyan subduction system in the tectonic evolution of the Lhasa Terrane and the Gangdese batholith thus represents an Andean-type magmatic arc along the Asian continental margin in the Lhasa Block before the Indian collision with Asia (Allegrè et al., 1984; Chung et al., 2005).

The magmatism in the northern belt is dominated by peraluminous, S-type granitoids (Xu et al., 1985; Harris et al., 1990; Kapp et al., 2005; Chung et al., 2005) and thus contrasts with the overwhelmingly I-type granitoids in the Gangdese belt. Recent work of Zhu et al. (2011) changed this simple picture. According to Zhu et al. (2011), the northern belt is comprised of magmatism in central and northern Lhasa subterranes. The central Lhasa subterrane was once a microcontinent with Archean basement where magmatism occurred from 240 Ma to 110 Ma. Most of these magmas are characterized by negative $\varepsilon_{Hf}(t)$, except for those of ~110 Ma showing positive $\varepsilon_{Hf}(t)$ (Chu et al., 2006; Zhu et al., 2011). The northern Lhasa subterrane is marked by magmatism between 135 and 110 Ma, with contemporaneous occurrence of metaluminous (I-type) and peraluminous (S-type) varieties. Collectively, available data show that igneous activity in the northern belt spanned over a relatively long period (240–110 Ma), with intensification during the early Cretaceous (Fig. 7a and b).

In addition to these major magmatic belts, intrusions in the Nyainqentanglha Range are worth mentioning. This range is situated north of the Gangdese batholiths. Geochronologic studies show that the Nyainqentanglha crystalline complex is composed of a number of granitoids ranging in age from Triassic to Late Miocene (Kapp et al., 2005a). Despite this wide age range, it has been shown that the intrusions were mainly emplaced during the Late Cretaceous–early Tertiary (Kapp et al., 2005a), i.e., roughly contemporaneous with the main phase of the Gangdese arc magmatism (Fig. 7a). Kapp et al. (2005a) argued that the Nyainqentanglha granites are of the Gangdese arc affinity. However, their published compositional data are indicative of a S-type granite and a derivation of old crustal source, with minor mantle input. A similar petrologic assessment has also been reached by Mitchell (1993).

6.2. Late Cretaceous-Paleogene magmatism in Burma

Two N–S trending magmatic belts are present in Burma. The western one, also called as the Cretaceous magmatic arc, is believed to be related to eastward subduction of Neo-Tethyan plate. It is located in the Burma microplate, west of the Sagaing fault, running from Sumatra and continuing through the Mogok belt into the Gangdese magmatic arc of Tibet (Mitchell, 1993). Magmatism in this belt includes Banmauk andesite and ophiolitic rocks and biotite-schists at Salingyi, which are intruded by granodioritic to tonalitic plutons and batholiths (Fig. 1a). Available data suggest that these rocks were emplaced during 115–74 Ma with low initial $^{87}Sr/^{86}Sr$ ratios around 0.705 (Darbyshire and Swainbank, 1988). To further south and east, the late Cretaceous I-type plutons and post-early Cretaceous diorites, granodiorites and volcanic rocks occur near Kyaukse (Garson et al., 1976). Barley et al. (2003) also identified Mid-Cretaceous to earliest Eocene (120–50 Ma) I-type granitoids in the MMB. All these suggest an up to 200 km wide magmatic arc belt extended along the Asian margin prior to the Indo-Asian collision (Barley et al., 2003).

Another belt, to the east of the Sagaing fault, extends from south of Mandalay southwards through the Shan Scarps and southwestern Burma into south Thailand. The intrusions in this belt range from granodiorite to leucogranite, with metaluminous to peraluminous features. Both I-type and S-type granites are present in this elongated belt, but S-type granites dominate, with which tin and tungsten deposits are associated (Cobbing et al., 1986; Zaw, 1990). Radiometric dating ranges from early Cretaceous to early Miocene with most being in the range of 45–59 Ma. Limited isotopic analyses indicate high initial $^{87}Sr/^{86}Sr$ ratios (>0.71; Cobbing et al., 1986; Darbyshire and Swainbank, 1988) suggest that they may have resulted from crustal thickening due to regional thrusting. Mitchell (1993) speculated that this belt partly overlaps with the MMB and the equivalent Mogok belt in Tibet is the Nyainqentanglha Range complex. However, northward continuation of this belt remains ambiguous in the region near the China–Burma border.

6.3. Magmatic affinity in the GTY area

The magmatism in the Gaoligong–Tengliang area is characterized by predominant S-type granitoids with emplacement ages ranging from Early Cretaceous, to late Cretaceous and early Cenozoic. I-type granites are only observed in the area near the China–Burma border, probably continue in Burma. Moreover, there is a younging trend oblique to the regional geological strike, from NE to SW. Despite the limited arc-related magmatism, the time–space variation in magmatism in the Gaoligong–Tengliang area is comparable to that in Tibet. Specifically, in terms of emplacement age, lithologic affinity and Hf isotopes (Figs. 7 and 8), the Gaoligong early Cretaceous granites resemble those in the Northern magmatic belt in the Lhasa Block and in Bomi–Chayu, whereas the late Cretaceous–Early Cenozoic I-type granites (and associated gabbroic intrusions) in western Yingjiang may be the equivalent of the Gangdese arc magmatism. The late Cretaceous–Early Cenozoic S-type, peraluminous granites in east Yingjiang and Tengliang area are reminiscent of the intrusions in the Nyainqentanglha Range (Kapp et al., 2005a). The dual presence of I-type and S-type granites of late Cretaceous and Paleogene age in the Tengliang and Yingjiang area confirms the Mitchell's speculation that they may represent northern continuation of late Cretaceous magmatic arc and N–S trending S-type granite belt in SE Asia.

To sum up, the similarity of the magmatism in the GTY area with that in Tibet lends support to the notion that the GTY area represents the rotated, eastern extension of the Lhasa Block. This area also represents the tectonic continuation of continental magmatic arc and parallel S-type granite belt in Burma. Nevertheless, some differences are noted between different terranes: (1) Magmas in the Central Lhasa subterrane are predominantly crustally derived, whereas in Northern and Southern Lhasa subterranes both I-type and S-type magmatism are present (Zhu et al., 2011). Equivalents of magmas in the Central and Southern Lhasa subterranes are present in the western Yunnan, however, those in the Northern Lhasa subterrane are not found in the studied area. In addition, although we interpret the late Cretaceous–Early Cenozoic I-type granites from west Yingjiang as arc-related, their ε_{Hf} values in zircons range from −4 to +6, significantly lower than those reported

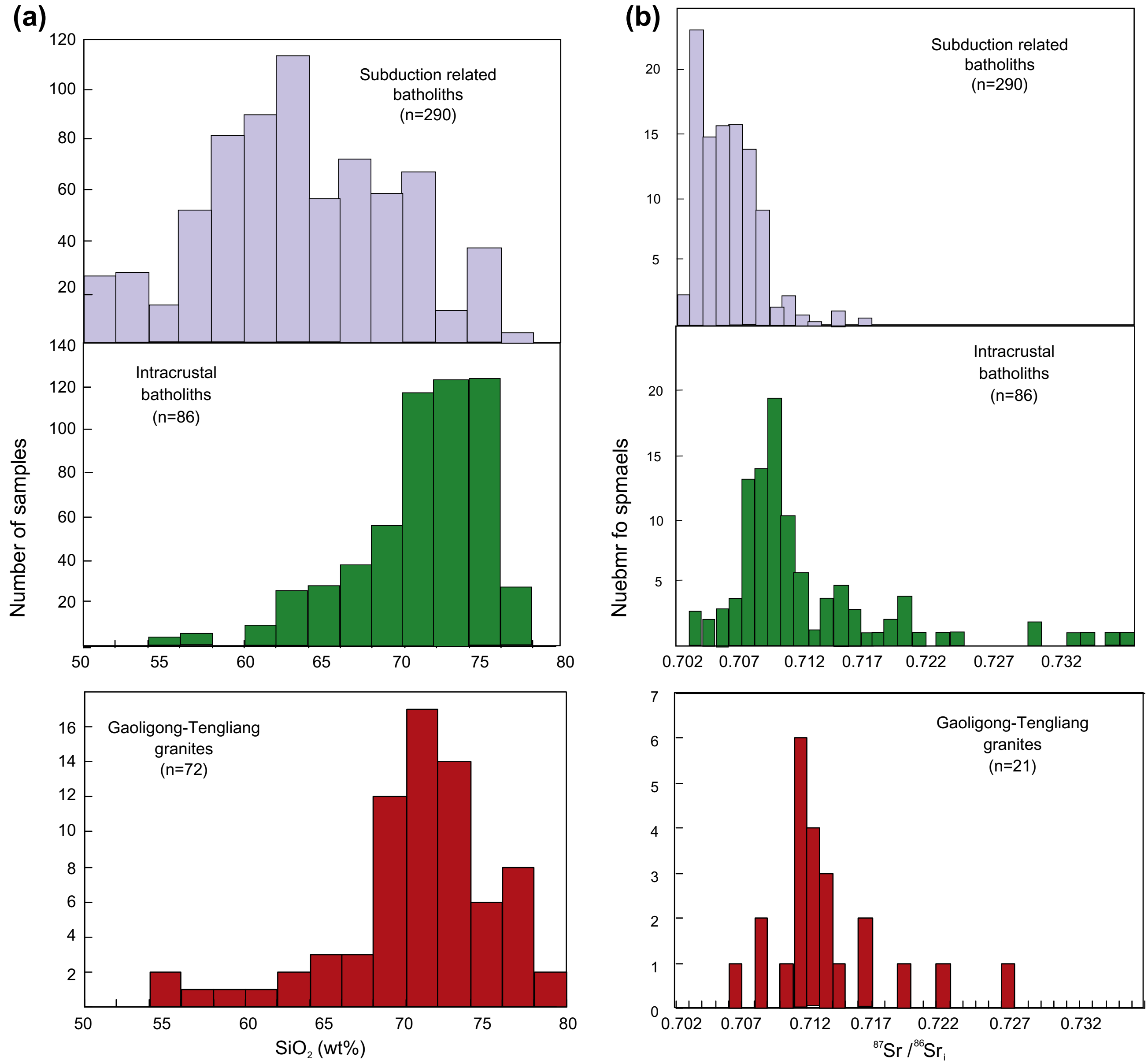

Fig. 10. Histograms comparing (a) the SiO_2 contents and (b) $^{87}Sr/^{86}Sr$ of granites from Gaoligong and Tengliang area with those known subduction-related batholiths and intracontinental batholiths. Data for subduction-related batholiths including Central Volcanic zone of the Andes Mountains, the Trans-Himalaya batholith of Asian, and data for intracontinental granitoid (North American Cordilleran Interior) are compiled by Driver et al. (2000) and De et al. (2000). Note that both Gaoligong and Tengliang granitoids are characterized by relatively high SiO_2 contents and $^{87}Sr/^{86}Sr$ ratios similar to the Cordilleran interior granitoids but distinctly unlike the continental arc granitoids. Data of SiO_2 content and $^{87}Sr/^{86}Sr$ are from Yang et al. (2006).

for the typical Gangdese arc magmas (up to +15, Fig. 8). This difference may be indicative of larger involvement of crustal components in arc magmatism in western Yingjiang relative to Gangdese magmatism, or location of true arc belt further west of the studied area. (2) While a semicontinuous N-S trending belt of extensive S-type granites occurs in Burma, Tengliang and Bomi–Chayu (Lin et al., this volume), equivalent rock types are only observed in the Nyainqentanglha Range, in the Lhasa terrane. (3) The Tengliang S-type granites were emplaced during 68–76 Ma, a period corresponding to the magmatic quiescence (70–80 Ma) in the Lhasa block (Fig. 7).

7. Petrogenetic assessment and discrimination of tectonic setting

Peraluminous granite is traditionally considered to be formed during continent–continent collisional events (LeFort, 1981; Pearce et al., 1984; Harris et al., 1990) or in a post-collisional setting after the climax of crustal thickening (Sylvester, 1998). In other words, peraluminous granites were formed in collision-related setting (Barbarin, 1999) rather than subduction-related and rift setting. However, conventional geochemical tectonic discrimination diagram (Pearce et al., 1984) does not yield consistent results. For example, in the Rb–Y + Nb plot, the Gaoligong early Cretaceous granites are mostly plotted in VAC field (Fig. 9a), suggesting a subduction-related setting. On the other hand, the same plot does not yield unambiguous information for the tectonic setting of the formation of the Tengliang granites, as they straddle the boundaries between within plate, volcanic arc and collisional granites (Fig. 9b). It has been argued that the chemical characteristics of granites are a direct consequence of the compositions of their source rocks and the condition of crustal melting. As such, there is no solid basis to use trace element composition for tectonic discrimination.

In the Gaoligong case, the intracontinental rifting setting for the Cretaceous and Early Tertiary batholiths can be ruled out given its peculiar tectonic situation. The possible tectonic scenario includes subduction and intracrustal thickening. The major difference in these two tectonic settings may be the extent of mantle involvement in crustal melting. Crustal melting and mixing caused by influx of mantle-derived magma are common in the subduction-related setting, but are rare in intracrustal setting. In order to evaluate these alternatives, we follow the approach of Driver et al. (2000) by comparing the Gaoligong–Tengliang–Yingjiang batholiths with known subduction-related magmatism and those formed in intracrustal settings. It has been shown that the subduction-related magmatism is characterized by a wide range in SiO_2 content from 50 to >70% (Fig. 10). Importantly a large proportion of samples from subduction-related settings have less than 64% SiO_2, coupled with relatively low $\delta^{18}O$ and $^{87}Sr/^{86}Sr$ and high ε_{Nd}, reflecting a significant mantle contribution to magmatism (Brandon and Smith, 1994; Driver et al., 2000). By contrast, the batholiths formed as a result of crustal thickening contain little or no tonalite, but are largely composed of muscovite- and biotite-bearing monzogranite and syenogranite and characterized by abundant S-type granites. They are more silicic than the subduction-related magmatism with SiO_2 content >65% and have almost exclusively negative ε_{Nd} values and $\delta^{18}O$ values (mainly >8.5%) (Driver et al., 2000). These crustally-derived S-type granites are interpreted as a result of intracrustal thickening due to regional fold-thrust deformation (Livaccari, 1991; Driver et al., 2000; Ducea, 2001).

In the Gaoligong–Tengliang area, the batholiths are dominated by monzogranite and granodiorites over tonalite and quartz diorite (Fig. 2a), the high SiO_2 content (>65%), negative ε_{Nd} and ε_{Hf} and high Sr isotopic ratios (Yang et al., 2006; This study), indicating a provenance from evolved crustal sources with insignificant mantle contribution (Fig. 10). The general lack of mantle contribution in the Gaoligong–Tengliang batholiths is not expected in a subduction-related setting, but is compatible with crustal thickening in an intracrustal setting.

Mantle contribution is evident for the granitoids from western Yingjiang, near the China–Burma border, given the positive zircon ε_{Hf} values (Fig. 6). This is consistent with their lithology of I-type granites and the presence of associated gabbroic intrusions (Fig. 1). This, together with their location proximal to the Burma arc belt, suggests a subduction-related magmatism.

8. Tectono-magmatic model(s)

8.1. Late Cretaceous-Paleogene granites: results of crustal melting in a Cordilleran-type setting

The late Cretaceous-Paleogene granitoids from Tengliang and Yingjiang apparently show a distinct distribution of rock types. Specifically the S-type granites are distributed to east, whereas the I-type granites (with associated mafic intrusions) exclusively occur in west Yingjiang. Such a distribution pattern is compatible with the two parallel magmatic belts in SE Asia, described in previous sections. The S-type and I-type magmatic belts are mirrored by their isotopes. For instance, available data show a positive ε_{Hf} in zircons (Fig. 6) for granitoids from western Yingjiang, whereas the overwhelmingly negative ε_{Hf} values for the Tengliang granites are indicative of little mantle contribution. In Burma, initial $^{87}Sr/^{86}Sr$ ratio of I-type granites (<0.705) is significantly lower than the contemporaneous S-type granites (>0.710, Darbyshire and Swainbank, 1988).

This observed chemical polarity is strongly reminiscent of that of the North American Cordillera which comprises a coastal belt typical of continental margin arcs and an inland peraluminous

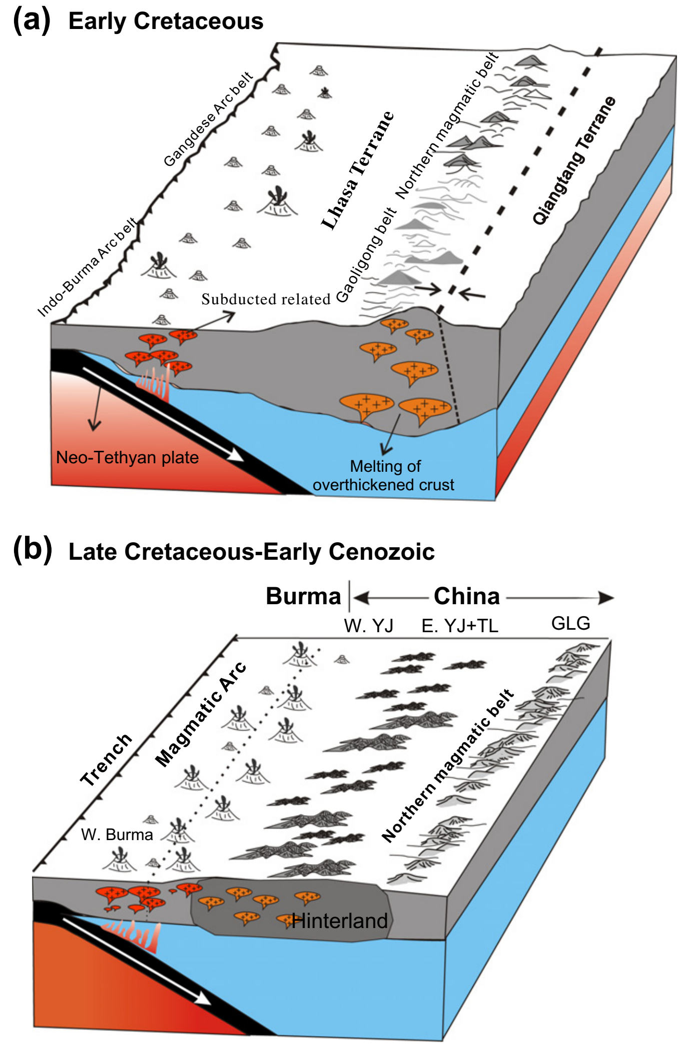

Fig. 11. Schematic illustration showing tectonic evolution in the GTY region. (a) During the early Cretaceous, the Gaoligong batholiths, equivalent to those in the northern magmatic belt in the Lhasa Terrane, were formed by melting of the overthickened crust due to the collision between the Lhasa Block and the Qiangtang Block and to the northward underthrusting of the Lhasa terrane beneath the Qiangtang terrane induced by a flat subduction of the Neo-Tethyan plate. The dashed line marks the Nujiang suture. (b) The late Cretaceous–early Cenozoic in Burma and SW China was characterized by the conjugation of the subduction of Neo-Tethyan plate and the collision between the west Burma plate and Sundalands. Combined effect of convergence-induced plate compressive forces and microcontinental collision resulted in crustal thickening of the hinterland, creating a belt of S-type granites. This belt is parallel with the magmatic arc belt related to the Neo-Tethyan subduction. The dashed line marks the boundary between west Burma and Sundaland. W. YJ = west Yingjiang; E. YJ = east Yingjiang; TL = Tengliang; GLG = Gaoligong.

granite belt (Fig. 10b; Mitchell, 1981; Pictcher, 1997; Driver et al., 2000; Ducea, 2001). It is also very similar to that observed in Southern and Central Lhasa subterranes (Zhu et al., 2011). We thus adopt a model similar to that proposed for the North American Cordilleran batholiths to explain the late Cretaceous–Early Cenozoic magmatism in the Tengliang and Yingjiang area and by inference, the origin of the extensive S-type granite in SE Asia (Fig. 11). The eastward subduction of the Neo-Tethys beneath the Asian continent generated a magmatic arc behind the fore-arc basin, now occurring in the China–Burma border, by slab fluid-assisted melting of mantle wedge. The batholiths in this arc belt were formed through a two-stage process, with underplating of mantle-derived magmas at the base of the crust, followed by melting of these underplates. In the hinterland behind the magmatic arc (i.e., Tengliang and east Yingjiang area), deep-seated conductive heating of crust and lithosphere induced by subduction may have progressively decreased crustal strength (Barton, 1990). Compressive plate-convergence forces then triggered crustal thickening and topographic uplift by telescoping the thermally weakened zone. Once maximum elevation is attained, the uplifted region may continue to grow laterally by over thrusting (Livaccari, 1991). This led to major deformation along the hinterland. The culmination of crustal thickening and subsequent extension collapse would have triggered the peraluminous magmatism.

A similar process is able to describe the magmatism in Gangdese arc and magmatism in the Nyainqentanglha Range in Tibet. The formation of the Gangdese magmatism was related to the Neo-Tethyan subduction underneath the Lhasa terrane and subsequent roll-back of Tethyan oceanic plate (Ding et al., 2003; Chung et al., 2005; Kapp et al., 2007a; Wen et al., 2008; Ji et al., 2009), while the S-type granites in the Nyainqentanglha Range may have been induced by crustal thickening. This Cordilleran-style model involves contrational deformation and fold-and-thrust in the continental arc margin and in the hinterland crust, which are observed in the field. For instance, Kapp et al. (2007b) identified a northward-propagating retroarc thrust belt operational between 105 and 53 Ma. They further estimated that the thrust belt could have accommodated >230 km (>55%) N–S shortening in the Lhasa Terrane. Growing evidence for crustal shortening predating the Indo-Asian collision areas of the Lhasa terrane has been documented (Tapponnier et al., 1982; Murphy et al., 2000; Kapp et al., 2005b, 2007a). If the crust under Tibet was 35 km thick prior to shortening, and the crustal volume is conserved, 50% shortening would have produced an average crustal thickness of >70 km. Under such a circumstance, the metasedimentary layer becomes hot enough to produce granitic magmas capable of rising into the upper crust (Patino Douce et al., 1990).

Crustal thickening and subsequent extensional collapse in the hinterland behind a subduction zone may be related to the rate of plate convergence (Livaccari, 1991). For example, the period of 70–80 Ma in Tibet was characterized by relatively low rate of convergence (Lee and Lawver, 1995) and a flat subduction which hampered the conductive heating from mantle to overriding crust. This explains the absence of subduction-related magmatism and S-type magmatism during this period. Since ca. 70 Ma, the rate of convergence increased dramatically (Lee and Lawver, 1995), probably correlated with a transition from flat to steep subduction (i.e., slab rollback). The steepening of subducting slab opened a window allowing the rising of asthenosphere, resulting in generation of late Cretaceous–Early Cenozoic Gangdese batholiths and Linzizong volcanism (Chung et al., 2005; Wen et al., 2008). The convection induced by slab rollback enhanced the conductive heating of hinterland crust, making crustal thickening favorable. The rate of convergence slowed down since ca. 60 Ma, thereby releasing the confined pressure and stress on thickened crust. As a consequence, extensional collapse took placed (Livaccari, 1991), generating voluminous peraluminous crustal melts, like those in the Nyanqentanglha Range.

The emplacement of the Tengliang granites took place at 66–76 Ma, a period corresponding to the magmatic quiescence in Tibet (Fig. 7). This may imply that the rate of convergence and geometry of Neo-Tethyan subduction are different in Tibet and in western Yunnan. Alternatively, while the subduction of Indian Oceanic plate beneath the Asian continent offers a long-term regional mechanism for late Mesozoic-early Cenozoic crustal deformation and magmatism in a Cordilleran-type setting, the geology of Burma and western Yunnan may also have been influenced by collisions between microcontinents. The Burma microplate collided with the western margin of the Sundaland block in the late Cretaceous-Paleogene (Cobbing et al., 1986; Zaw, 1990; Mitchell, 1993). Key evidence for this late Cretaceous-Paleogene collision includes a high-temperature, low-pressure amphibolite-facies metamorphic event (84 Ma) recognized in orthogneisses from western Thailand (Dunning et al., 1995) and Eocene (47–43 Ma) high-grade metamorphism recorded in rims to Jurassic zircons in some intrusions with the MMB (Barley et al., 2003).

8.2. Early Cretaceous granites: products of collision-induced crustal thickening

The early Cretaceous granitoids from Gaoligong share similarities of emplacement age and geochemistry with that in Bomi–Chayu area (Chiu et al., 2009; Lin et al., this volume) and in the northern magmatic belt in Tibet (Xu et al., 1985). As such, the data of the Gaoligong belt provide insights into the formation of the northern magmatic belt, which remains controversial and has been attributed to (1) low-angle northward subduction of Neo-Tethys oceanic lithosphere (Coulon et al., 1986; Ding et al., 2003); (2) southward subduction of the Bangong–Nujiang oceanic slab (Zhu et al., 2009, 2011); (3) melting of overthickened crust due to Lhasa-Qiangtang continental collision (Xu et al., 1985; Pearce and Mei, 1988), or crustal anatexis related to mantle attenuation and associated asthenospheric upwelling following Lhasa-Qiangtang continental collision (Harris et al., 1990); (4) northward underthrusting of the Lhasa terrane beneath the Qiangtang terrane along the Bangong suture during low-angle subduction of Neo-Tethys oceanic lithosphere (Kapp et al., 2005b).

Both peraluminous nature and the lack of significant involvement of mantle components in crustal melting (Figs. 2 and 8) argue against a process directly related to subduction for the genesis of the Gaoligong granitoids. In principle, the model proposed for the late Cretaceous–early Cenozoic S-type granites can equally be applied to explain the generation of early Cretaceous plutons, given the long-lasting subduction of the Neo-Tethyan plate that started since as early as Jurassic (Barley et al., 2003; Chu et al., 2006; Searle et al., 2007). The problem with this model is that subduction-induced crustal thickening in the hinterland propagates with time away from the trench (Livaccari, 1991), whereas the time–space variation in magmatism observed in the Gaoligong and Tengliang area delineates an opposite trend.

It is likely that the early and late Cretaceous granites were formed in two different tectonic regimes. The former was related to collision-induced crustal thickening in a post-collisional regime (Xu et al., 1985; Pearce and Mei, 1988), the latter was related to crustal thickening induced by far-field forces transmitting from Neo-Tethyan subduction. The localization of early Cretaceous S-type granites proximal to the Nujiang suture suggests that the crustal thickening was likely related to the Lhasa-Qiangtang collision. This finds its additional evidence from duration of magmatism. Patino Douce et al. (1990) modeled the effect of thrusting and associated thickening on geothermal gradients. They suggested that thickening of 1.5–2 times the original crustal thickness resulted in widespread anatexis at middle and lower crustal levels and also predicted main phase of magmatism begins 5–25 Ma after the cessation of crustal thickening. The collision between the Lhasa Terrane and the Qiangtang Block took place during the late Jurassic and Earliest Cretaceous (Dewey et al., 1988; Kapp et al., 2005b, 2007a). The emplacement age (130–120 Ma) obtained in this study show that the Gaoligong peraluminous granites were emplaced 10–20 Ma after the collision event, thus consistent with the modeling results.

Though concentrated in early Cretaceous, S-type granitic magmatism spanned over Jurassic and early Cretaceous (Chu et al., 2006; Zhu et al., 2011). While this igneous longetivity is not easily accommodated with the post-collisional model (Chiu et al., 2009;

Lin et al., this volume), it cannot be used either as an argument to rule out the model, because magmas of different ages in a given area could have been generated under different tectonic regimes. In the studied area, there is a distinct time–space variation in S-type magmatism, that is, the late Cretaceous-Paleogene S-type granites are apparently bounded to east by the early Cretaceous S-type granites and to south by contemporaneous Gangdese arc. As mentioned earlier, the late Cretaceous-Paleogene S-type granites may not necessarily be related to the early Cretaceous in genesis. We thus argue that, the igneous longetivity may reflect overprints of a post-Lhasa/Qiangtang collisional regime by "far-field" influence of the Neo-Tethyan subduction (Fig. 11).

9. Conclusions

(1) Both the Gaoligong and Tengliang batholiths are dominated by biotite-bearing granite/leucogranite and granodiorites with very minor amount of tonalite. They are peraluminous and strongly peraluminous and have negative zircon ε_{Hf}, indicating little mantle contribution. They were likely derived from partial melting of Mesoproterozoic sedimentary rocks. Only a small portion of plutons in the southwestmost of the study region (Yingjiang), proximal to the China–Burma border are of I-type granites, indicating various extent of mantle contribution.

(2) Zircon U–Pb dating reveals three distinct episodes of magmatism that migrate from NE to SW. While the Gaoligong granites (northeast) were mainly emplaced during early Cretaceous (121–126 Ma), the Tengliang granites, situated southwest to the Gaoligong belt, were emplaced in late Cretaceous (68–76 Ma). The youngest event (52–56 Ma) occurred in the Yingjiang area, southwestmost of the study region.

(3) The late Cretaceous–early Cenozoic plutons in Tengliang and Yingjiang are the northern continuation of the late Cretaceous magmatic arc (west) and the belt of predominant S-type granites (east) in SE Asian (Thailand, Burma). This distribution pattern resembles that in Tibet with a southern Gangdese arc belt and a less well developed belt of S-type granites exemplified by the Nyainqentanglha Range. Strongly reminiscent of the northern American Cordillera, such a chemical polarity indicates a Cordilleran-style setting for the late Cretaceous–early Cenozoic plutonism in the Tengliang-Yingjiang area. While the magmatic arc was related to eastward subduction of the Neo-Tethys beneath the Asian continent, the S-type granites represent crustal melting in the hinterland in response to crustal thickening triggered by subduction-induced decrease in lithospheric strength and compressive plate-convergence forces and to less degrees by collisions of microcontinents.

(4) The early Cretaceous Gaoligong granitoids bear strong similarities to those in the northern magmatic belt in the Lhasa Terrane, which is the magmatic expression of crustal thickening. This crustal thickening may have resulted from the collision between the Lhasa Block and the Qiangtang Block in late Jurassic and Early Cretaceous.

Acknowledgements

This study was financially supported by the CAS/SAFEA International Partnership Program for Creative Research Teams, the Ministry of Science and Technology China (2002CB412603 and 2011CB808906) and National Science Foundation of China (70914001). This is GIG Publication No. 1418.

References

Aitchison, J.C., Ali, J.R., Davis, A.M., 2007. When and where did Indian and Asian collide? Journal of Geophysical Research-Solid Earth 112. doi:10.1029/2006JB004706.

Allegrè, C.J. et al., 1984. Structure and evolution of the Himalaya–Tibet orogenic belt. Nature 307, 17–22.

Barbarin, B., 1999. A review of the relationships between granitoid types, their origins and their geodynamic environments. Lithos 46, 605–626.

Barley, M.E., Pickard, A.L., Zaw, K., Rak, P., Doyle, M.G., 2003. Jurassic to Miocene magmatism and metamorphism in the Mogok metamorphic belt and the India–Eurasia collision in Myanmar. Tectonic 22, 1019. doi:10.1029/2002TC001398.

Barton, M.D., 1990. Cretaceous magmatism, metamorphism, and metallogeny in the east-central Great Basin. In: Anderson, J.L., (ed.), The Nature and Origin of Cordilleran Magmatism. Geological Society of America Memoir 174, 283–302.

Blichert-Toft, J., Albarede, F., 1997. The Lu-Hf isotope geochemistry of chondrites and the evolution of the mantle-crust system. Earth and Planetary Science Letters 148, 243–253.

Booth, A.L., Zeitler, P.K., Kidd, W.S.F., Wooden, J., Liu, Y.P., Idleman, B., Hren, M., Chamberlain, P., 2004. U–Pb zircon constraints on the tectonic evolution of southeastern Tibet, Namche Barwa area. American Journal of Science 304, 889–929.

Brandon, A.D., Smith, A.D., 1994. Mesozoic granitoid magmatism in southeast British-Columbia – implications for the origin of granitoid belts in the north American Cordillera. Journal of Geophysical Research 99, 11879–11896.

Chen, Z., Burchfiel, B.C., Liu, Y., King, R.W., Royden, L.H., Tang, W., Wang, E., Zhao, J., Zhang, X., 2000. Global Positioning System measurements from eastern Tibet and their implications for India/Eurasia intercontinental deformation. Journal of Geophysical Research 105 (B7), 16215–16227.

Chen, F., Satir, M., Ji, J., Zhong, D., 2002. Nd–Sr–Pb isotopes of Tengchong Cenozoic volcanic rocks from western Yunnan, China: evidence for an enriched-mantle source. Journal of Asian Earth Sciences 21, 39–45.

Chiu, H.Y., Chung, S.L., Wu, F.Y., Liu, D.Y., Liang, Y.H., Lin, Y.J., Iizuka, Y., Xie, L.W., Wang, Y.B., Chu, M.F., 2009. Zircon U–Pb and Hf isotope constraints from eastern Trans-Himalayan batholiths on the precollisional magmatic and tectonic evolution in southern Tibet. Tectonophysics 477, 3–19.

Chu, M.F., Chung, S.L., Song, B., Liu, D.Y., O'Reilly, S.Y., Pearson, N.J., Ji, J.Q., Wen, D.J., 2006. Zircon U–Pb and Hf isotope constraints on the Mesozoic tectonics and crustal evolution of southern Tibet. Geology 34, 745–748.

Chung, S.-L., Lo, C.-H., Lee, T.-Y., Zhang, Y.-Q., Xie, Y.-W., Li, X.-H., Wang, K.-L., Wang, P.-L., 1998. Diachronous uplift of the Tibetan plateau starting 40 Myr ago. Nature 394, 769–773.

Chung, S.-L., Chu, M.F., Zhang, Y.Q., et al., 2005. Tibet tectonic evolution inferred from spatial and temporal variations in post-collisional magmatism. Earth Science Review 68, 173–196.

Cobbing, E.J., Mallick, D.I.J., Pitfield, P.E.J., Teoh, L.H., 1986. The granites of the Southeast Asian Tin belt. Journal of Geology Society London 143, 537–550.

Coulon, C., Maluski, H., Bollinger, C., 1986. Mesozoic and Cenozoic volcanic rocks from central and southern Tibet: ^{39}Ar–^{40}Ar dating, petrological characteristics and geodynamical significance. Earth and Planetary Science Letters 79, 281–302.

Darbyshire, D.P.F., Swainbank, I.G., 1988. Geochronology of a Selected Granite From Burma. NERC Isotope Geology Center Report No. 88/6.

De, S.K., Chacko, T., Creaser, R.A., Muehlenbachs, K., 2000. Geochemical and Nd-Pb-O isotope systematics of granites from the Talson Magmatic Zone, NE Alberta: implications for early Proterozoic tectonics in western Laurentia. Precambrian Research 102, 221–249.

Debon, F., Le Fort, P., Sheppard, S.M.F., 1985. The four plutonic belts of the Transhimalaya: a chemical, mineralogical, isotopic, and chronological synthesis along a Tibet–Nepal section. Journal of Petrology 27, 219–250.

Dewey, J.F., Shackelton, R.M., Chang, C., Sun, Y., 1988. The tectonic evolution of the Tibetan Plateau. Philosophical Transactions of the Royal Society of London A327, 379–413.

Ding, L., Kapp, P., Yin, A., Deng, W.-M., Zhong, D.-L., 2003. Early Tertiary volcanism in the Qiangtang terrane of central Tibet: evidence for a transition from oceanic to continental subduction. Journal of Petrology 44, 1833–1865.

Driver, L.A., Creaser, R.A., Chacko, T., Erdmer, P., 2000. Petrogenesis of the Cretaceous Cassiar batholith, Yukon–British Columbia, Canada: implications for magmatism in the North American Cordilleran Interior. Geological Society of America Bulletin 112, 1119–1133.

Ducea, M.N., 2001. The California arc: thick granite batholiths, eclogitic residues, lithospheric scale thrusting, and magmatic flare-ups. Geological Society of America Today 11, 4–10.

Dunning, G.R., MacDonald, A.S., Barr, S.M., 1995. Zircon and monazite U–Pb dating of the Doi Inthanon core complex, northern Thailand: implications for extension within the Indosinian Orogen. Tectonophysics 251, 197–213.

Garson, M.S., Amos, B.J., Mitchell, A.H.G., 1976. The Geology of the Country around Neyaunggya and Tengan, South Shann States, Burma. Institute of Geological Sciences, Overseas Memoires, 2, HMSO, London.

Griffin, W.L., Pearson, N.J., Belousova, E.A., Saeed, A., 2006. Comment: Hf-isotope heterogeneity in standard zircon 91500. Chemical Geology 233, 358–363.

Harris, N.B.W., Inger, S., Xu, R.H., 1990. Cretaceous plutonism in Central Tibet – An example of postcollision magmatism. Journal of Volcanology and Geothermal Research 44, 21–32.

Harrison, T.M., Copeland, P., Kidd, W.S.F., Yin, A., 1992. Raising Tibet. Science 255, 1663–1670.

Hoskin, P. W. O., Schaltegger, U. 2003. The composition of zircon and igneous and metamorphic petrogenesis. In: Zircon. Hanchar, J. M., Hoskin, P.W.O., eds., Reviews in Mineralogy and Geochemistry 53, 27-55.

Hughes, R.W., Galibert, O., Bosshart, G., 2000. Burmese jade: the inscrutable gem. Gems and Geomology 36, 2–26.

Ji, W.-Q., Wu, F.-Y., Chung, S.-L., et al., 2009. Zircon U–Pb chronology and Hf isotopic constraints on the petrogenesis of Gangdese batholiths, southern Tibet. Chemical Geology 262, 229–245.

Kapp, J.L.D., Harrison, T.M., Grove, M., Lovera, O.M., Lin, D., 2005a. Nyainqentanglha Shan: a window into the tectonic, thermal, and geochemical evolution of the Lhasa block, southern Tibet. Journal of Geophysical Research 110, B08413. doi:10.1029/2004JB003330.

Kapp, P., Yin, A., Harrison, T.M., Ding, L., 2005b. Cretaceous–Tertiary shortening, basin development, and volcanism in central Tibet. Geological Society of America Bulletin 117, 865–878.

Kapp, P., DeCelles, P.G., Gehrels, F.E., Heizler, M., Ding, L., 2007a. Geological records of the Lhasa–Qiangtang and Indo–Asian collisions in the Nima area of Central Tibet. Geological Society of America Bulletin 119, 917–932. doi:10.1130/.B26055.1.

Kapp, P., DeCelles, P.G., Leier, A.L., Fabijanic, J.M., He, S., Pullen, A., Gehrels, F.E., Ding, L., 2007b. The Gangdese Retroarc thrust belt revealed. Geological Society of America Today 17. doi:10.1130/GSAT01707A.1.

Lee, T.-Y., Lawver, L.A., 1995. Cenozoic plate reconstruction of Southeast Asia. Tectonophysics 251, 85–138.

Lee, H.-Y., Chung, S.L., Wang, J.R., 2003. Miocene Jiali faulting and implications for Tibet tectonic evolution. Earth and Planetary Science Letters 205, 185–194.

LeFort, P., 1981. Manaslu leucogranite – A collision signature of the Himalaya a model for its genesis and emplacement. Journal of Geophysical Research 86, 545–568.

Li, P., Gao, R., Cui, J.W., Guan, Y., 2004. Paleomagnetic analysis of eastern Tibet: implications for the collisional and amalgamation history of the Three Rivers Region, SW China. Journal of Asian Earth Sciences 24, 291–310.

Liang, H.Y., Chung, S.L., Liu, D.Y., et al., 2008. Detrital zircon evidence for Burma for re-organization of the eastern Himalayan river system. American Journal of Science 308, 618–638.

Livaccari, R.F., 1991. Role of crustal thickening and extensional collapse on the tectonic evolution of the Sevier-Laramide orogeny, western United States. Geology 19, 1104–1107.

Ludwig, K.R., 2001a. Squid 1.02, in A User Manual, Berkeley. Berkeley Geochronological Center Special Publication, 1-219.

Ludwig, K.R., 2001b. Using Isoplot/EX, Version 2.49, in A Geolocronolgical Toolkit for Microsoft Excel, Berkeley. Berkeley Geochronological Center Special Publication, 1-55.

Metcalfe, I., 1998. Palaeozoic and Mesozoic geological evolution of the SE Asian region multidisciplinary constraints and implications for biogeography. In: Hall, R., Blundell, D. (Eds.), Biogeography and Geological Evolution of SE Asia. Backhuys Publishers, Amsterdam, The Netherlands, pp. 25–41.

Mitchell, A.H.G., 1981. Phanerozoic plate boundaries in Mainland Se Asian, The Himalayas and Tibet. Journal of Geology Society London 138, 109–122.

Mitchell, A.H.G., 1993. Cretaceous–Cenozoic tectonic events in the western Myanmar (Burma) – Assam region. Journal of Geology Society London 150, 1089–1102.

Morley, C.K., 2004. Nested strike-slip duplexes, and other evidence for Late Cretaceous–Palaeogene tranpressional tectonics before and during India-Eurasia collision, in Thailand, Myanmar and Malaysia. Journal of Geology Society London 161, 799–812.

Murphy, M.A., Yin, A., Kapp, P., et al., 2000. Southward propagation of the Karakoram fault system, southwest Tibet: timing and magnitude of slip. Geology 28, 451–454.

Pan, G.T., Ding, J., Yao, D., Wang, L., 2004. The Guide Book of 1:1500,000 Geological Map of the Qinghao-Xizang (Tibet) Plateau and Adjacent Areas. Chengdu Cartographic Publication House, 48p.

Patino Douce, A.E., Humphreys, D.E., Johnston, A.D., 1990. Anatexis and metamorphism in tectonically thickened crust exemplified by the Sevier Hinterland, Western North America. Earth and Planetary Science Letters 97, 290–315.

Pearce, J.A., Mei, H., 1988. Volcanic rocks of the 1985 Tibet Geotraverse: Lhasa to Golmud. Philosophical Transactions of the Royal Society of London A327, 169–201.

Pearce, J.A., Harris, N.B.W., Tindle, A.G., 1984. Trace element discrimination diagrams for tectonic interpretation of the granitic rocks. Journal of Petrology 25, 956–983.

Pictcher, W.S., 1997. The Nature and Origin of Granite. Chapaman & Hall, 387pp.

Rowley, D., 1996. Age of initiation of collision between India and Asia: a review of stratigraphic data. Earth and Planetary Science Letters 145, 1–13.

Scharer, U., Xu, R.H., Allegre, C.J., 1984. U–Pb geochronology of Gangdese (Transhimalaya) Plutonism in the Lhasa-Xigaze region, Tibet. Earth and Planetary Science Letters 69, 311–320.

Searle, M.P., 1996. Geological evidence against large-scale pre-Holocene offsets along the Karakoram Fault: implications for the limited extrusion of the Tibetan plateau. Tectonics 15, 171–186.

Searle, M.P., Windley, B.F., Coward, M.P., et al., 1987. The closing of Tethys and the tectonics of the Himalaya. Geological Society of America Bulletin 98, 678–701.

Searle, M.P., Noble, S.R., Cottle, J.M., Wales, D.J., Mitchell, A.H.G., Hlaing, T., Horstwood, M.S.A., 2007. Tectonic evolution of the Mogok metamorphic belt, Burma (Myanmar) constrained by U–Th–Pb dating of metamorphic and magmatic rocks. Tectonics, 26, TC3014. doi:10.1029/2006TC002083.

Soderlund, U., Patchett, P.J., Vervoort, J.D., Isachsen, C.E., 2004. The ^{176}Lu decay constant determined by Lu–Hf and U–Pb isotope systematics of Precambrian mafic intrusions. Earth and Planetary Science Letters 219, 311–324.

Streckeisen, A., Le Maitre, R.W., 1979. A chemical approximation to the modal QAPF classification of the igneous rocks. Neues Jahrbuch fur Mineralogie, Abhandlungen 136, 169–206.

Sylvester, P.J., 1998. Post-collisional strongly peraluminous granites. Lithos 45, 29–44.

Tapponnier, P., Peltzer, G., Armijo, R., Le Dain, A., Cobbold, P., 1982. Propagating extrusion tectonics in Asia: new insights from simple experiments with plasticine. Geology 10, 611–616.

Tapponnier, P., Xu, Z., Roger, F., Meyer, B., Arnaud, N., Wittlinger, G., Yang, J., 2001. Oblique stepwise rise and growth of the Tibet plateau. Science 294, 1671–1677.

Turner, S., Hawkesworth, C.J., Liu, J., Rogers, N., Kelley, S., van Calsteren, P., 1993. Timing of Tibetan uplift constrained by analysis of volcanic rocks. Nature 364, 50–54.

Turner, S., Arnaud, N., Liu, J., Rogers, N., Hawkesworth, C., Harris, N., Kelley, S., van Calsteren, P., Deng, W.-M., 1996. Post-collisional, shoshonitic volcanism on the Tibetan plateau: implications for convective thinning of the lithosphere and the source of ocean island basalts. Journal of Petrology 37, 45–71.

Vervoort, J.D., Blichert-Toft, J., 1999. Evolution of the depleted mantle: Hf isotope evidence from juvenile rocks through time. Geochimica et Cosmochimica Acta 63, 533–556.

Wang, Q., Zhang, P.Z., Freymueller, J.T., et al., 2001. Present-day crustal deformation in China constrained by global positioning system measurements. Science 294, 574–577.

Wang, Y.J., Fan, W.M., Zhang, Y.H., Peng, T.P., Cheng, X.Y., Xu, Y.G., 2006. Early Oligocene rotational extrusion on the east of India: structural and ^{40}Ar/^{39}Ar geochronological evidences from the ductile fault systems surrounding southeastern Tibetan syntaxis (western Yunnan). Tectonophysics 418, 235–254.

Wen, D.R., Liu, D.Y., Chung, S.L., Chu, M.F., Ji, J.Q., Zhang, Q., Song, B., Lee, T.Y., Yeh, M.W., Lo, C.H., 2008. Zircon SHRIMP U–Pb ages of the Gangdese batholith and implications for Neotethyan subduction in southern Tibet. Chemical Geology 252, 191–201.

Williams, I., 1998. U–Th–Pb geochronology by ion microprobe. In: McKibben, M.A., Shanks, W.C., III, Ridley, W.I. (Eds.), Applications of Microanalytical Techniques to Understanding Mineralizing Processes. Reviews in Economic Geology, vol. 7, pp. 1–35.

Wu, F.-Y., Yang, Y.-H., Xie, L.-W., Yang, J.-H., Xu, P., 2006. Hf isotopic compositions of the standard zircons and baddeleyites used in U–Pb geochronology. Chemical Geology 234, 105–126.

Wu, F.Y., Huang, B.C., Ye, K., Fang, A.M., 2008. Collapsed Himalaya–Tibetan orogen and the rising Tibetan Plateau. Acta Petrolgica Sinica 24, 1–30.

Xu, R.-H., Schärer, U., Allègre, C.-J., 1985. Magmatism and metamorphism in the Lhasa block (Tibet): a geochronological study. Journal of Geology 93, 41–57.

Xu, Y.G., Lan, J.B., Yang, Q.J., Huang, X.L., Qiu, H.N., 2008. Eocene break-off of the Neo-Tethyan slab as inferred from intraplate-type basaltic dykes in the Gaoligong belt, eastern Tibet. Chemical Geology 255, 439–453.

Yang, Q.-J., Xu, Y.-G., Huang, X.-L., Luo, Z.-Y., 2006. Geochronology and geochemistry of granites in the Gaoligong tectonic belt, western Yunnan: tectonic implications. Acta Petrologica Sinica 22, 817–834.

Yin, A., Harrison, T.M., 2000. Geologic evolution of the Himalayan–Tibetan orogen. Annual Review of Earth and Planetary Sciences 28, 211–280.

Yin, A., Nie, S.Y., 1996. A Phanerozoic palinspastic reconstruction of China and its neighboring regions. In: Yin, A., Harrison, M. (Eds.), The Tectonic Evolution of Asia. University Press, Cambridge, pp. 442–484.

Yuan, H.L., Gao, S., Liu, X.M., Li, H.M., Günther, D., Wu, F.Y., 2004. Precise U–Pb age and trace element determinations of zircon by laser ablation-inductively coupled plasma mass spectrometry. Geostandards and Geoanalytical Research 28, 353–370.

Zaw, K., 1990. Geological, petrological and geochemical characteristics of granitoid rocks in Burma: with special reference to the associated W–Sn mineralisation and their tectonic setting. Journal of Southeast Asian Earth Sciences 4, 293–335.

Zhong, D.L., Ji, J.Q., Hu, S.L., 1999. The subduction age of Tethyan oceanic crust: the ^{40}Ar/^{39}Ar microarea dating of metamorphic residual oceanic crust. Chinese Science Bulletin 44, 1782–1785 (in Chinese).

Zhu, B.-Q., Mao, C.-X., Lugmair, G.W., Macdougall, J.M., 1983. Isotopic and geochemical evidence for the origin of Plio-Pleistocene volcanic rocks near the Indo-Eurasian collisional margin at Tengchong, China. Earth and Planetary Science Letters 65, 263–275.

Zhu, D.C., Mo, X.X., Niu, Y., et al., 2009. Geochemical investigation of Early Cretaceous igneous rocks along an east–west traverse throughout the central Lhasa Terrane, Tibet. Chemical Geology 268, 298–312.

Zhu, D.C., Zhao, Z.D., Niu, Y., et al., 2011. The Lhasa terrane: record of a micro-continent and its histories of drift and growth. Earth and Planetary Science Letters 301, 241–255.